

CLOUD AND STAR FORMATION IN DISK GALAXY MODELS WITH FEEDBACK

RAHUL SHETTY^{1,2} AND EVE C. OSTRIKER¹

Received 2008 March 4; accepted 2008 May 24

ABSTRACT

We include feedback in global hydrodynamic simulations in order to study the star formation properties, and gas structure and dynamics, in models of galactic disks. In previous work we studied the growth of clouds and spiral substructure due to gravitational instability. We extend these models by implementing feedback in gravitationally bound clouds; momentum (due to massive stars) is injected at a rate proportional to the star formation rate. This mechanical energy disperses cloud gas back into the surrounding interstellar medium, truncating star formation in a given cloud and raising the overall level of ambient turbulence. Propagating star formation can however occur as expanding shells collide, enhancing the density and triggering new cloud and star formation. By controlling the momentum injection per massive star and the specific star formation rate in dense gas, we find that the negative effects of high turbulence outweigh the positive ones, and *in net*, feedback reduces the fraction of dense gas and, thus, the overall star formation rate. The properties of the large clouds that form are not, however, very sensitive to feedback, with cutoff masses of a few million M_{\odot} , similar to observations. We find a relationship between the star formation rate surface density and the gas surface density with a power-law index ~ 2 for our models with the largest dynamic range, consistent with theoretical expectations for our model of disk flaring. We point out that the value of the “Kennicutt-Schmidt” index found in numerical simulations (and likely in nature) depends on the thickness of the disk, and therefore, a self-consistent determination must include turbulence and resolve the vertical structure. With our simple feedback prescription (a single combined star formation event per cloud), we find that global spiral patterns are not sustained; less correlated feedback and smaller scale turbulence appear to be necessary for spiral patterns to persist.

Subject headings: galaxies: ISM — ISM: clouds — ISM: kinematics and dynamics — stars: formation — turbulence

Online material: color figures

1. INTRODUCTION

A crucial intermediary for the formation of stars in the interstellar medium (ISM) is the gaseous cloud. Stars form deep within giant molecular clouds (GMCs), and GMCs themselves may be embedded in larger molecular and atomic structures, which are referred to as giant molecular associations (GMAs) and superclouds (Vogel et al. 1988; Elmegreen & Elmegreen 1983). The dispersal of cloud gas, resulting from the ionizing radiation from newly born stars, stellar winds, and supernovae (SNe), limits the lifetimes of GMCs and, therefore, determines their net star formation efficiencies. SNe also play a significant role in maintaining and/or determining the thermal phase balance of the ISM (Cox & Smith 1974; McKee & Ostriker 1977; Norman & Ikeuchi 1989; de Avillez & Breitschwerdt 2004), and simple estimates suggest that SNe may be the main source of turbulence, at least in the diffuse ISM (e.g., Spitzer 1978; Mac Low & Klessen 2004). Turbulence in both the diffuse and dense ISM is in turn considered one of the primary mechanisms regulating star formation (e.g., Elmegreen & Scalo 2004; Ballesteros-Paredes et al. 2007; McKee & Ostriker 2007). Since feedback from star formation is linked to the formation, evolution, and destruction of GMCs, the overall process may be self-regulating.

The formation and growth of clouds depend on the gravitational stability of the diffuse gaseous environment. In disk galaxies, galactic rotation and thermal pressure, among other factors, act to oppose the growth of self-gravitating perturbations. The

Toomre Q parameter indicates the susceptibility of axisymmetric perturbations to grow in uniform thin disks; for $Q < 1$, the surface density is sufficiently large for gas self-gravity to overwhelm the restoring effects of Coriolis forces and pressure (Toomre 1964). Nonlinear simulations have shown that for nonaxisymmetric perturbations and including the effects of disk thickness and stellar gravity, the threshold is $Q \approx 1.5$ (Kim et al. 2002; Kim & Ostriker 2001, 2007; Li et al. 2005b). The observed drop-off in star formation activity traced by $H\alpha$ at large radii supports the idea that stars preferentially form in gravitationally unstable regions with densities above a critical value (Kennicutt 1989; Martin & Kennicutt 2001).³ In general, magnetic fields cannot prevent but only slow the collapse of gas. In conjunction with other physical mechanisms, magnetic fields may in fact enhance instability, as is the case when the magnetorotational instability (Kim et al. 2003) is present, or via the magneto-Jeans instability (Kim et al. 2002).

Star formation must commence soon after the gas accumulates to form massive clouds, because almost all GMCs contain stars (Blitz et al. 2007). Ionizing radiation from newly formed stars subsequently dissociates the molecules, and $H\ II$ region expansion disperses the surrounding gas; some fraction of the gas may remain molecular, but in unbound clouds. The massive O and B stars reach the end of their lifetimes in ~ 2 – 20 Myr, with those over $8 M_{\odot}$ ending as SNe. The cumulative effect of feedback from all the contiguously forming stars contributes to the short estimated GMC lifetimes of ~ 20 Myr (e.g., Blitz et al. 2007).

¹ Department of Astronomy, University of Maryland, College Park, MD 20742; ostriker@astro.umd.edu.

² Harvard-Smithsonian Center for Astrophysics, 60 Garden Street, Cambridge, MA 02138; rshetty@cfa.harvard.edu.

³ Deep $H\alpha$ (Ferguson et al. 1998) and UV observations (Thilker et al. 2007; Boissier et al. 2007) indicate that a fraction of spiral galaxies have extended outer-disk star formation, but at much lower levels than in inner disks. In high- Q environments, clouds may grow to become self-gravitating by successive inelastic collisions.

The feedback from star formation could potentially prevent the formation of stars in nearby regions by driving turbulence and dispersing gas, but it could potentially trigger collapse events as well. Collisions between SN blast waves can result in sufficiently large densities for gas to collapse and form stars. It is not yet understood whether (or when) “positive” or “negative” feedback effects dominate; exploring this issue is one of the goals of the present work.

Despite the host of processes that impact the formation of stars, observations have shown a clear correlation between the star formation rate density Σ_{SFR} and the gas surface density Σ , with power-law forms (in actively star-forming regions)

$$\Sigma_{\text{SFR}} \propto \Sigma^{1+p}, \quad (1)$$

now known as Kennicutt-Schmidt laws (Schmidt 1959; Kennicutt 1998b). Power-law indices with $1 + p \approx 1-2$ have been found, depending on whether the total gas mass or just the molecular gas mass is included in Σ (e.g., Bigiel et al. 2008; Wong & Blitz 2002; Heyer et al. 2004; Schuster et al. 2007; Kennicutt et al. 2007; Bouche et al. 2007). These relations have been identified for a wide range of disk galaxies at low and high redshifts. Both global and local versions of the $\Sigma_{\text{SFR}}-\Sigma$ relations have been explored. In the former, surface densities are globally averaged within some outer radius; in the latter, averages are over radial annuli or smaller regions. A second empirical law obtained by Kennicutt is $\Sigma_{\text{SFR}} \approx 0.1 \Sigma / t_{\text{orb}}$, where t_{orb} is the local orbital time of the gas.

Many theoretical studies have attempted to explain the observed relations between the star formation rate and the gas surface density. Simple analytic prescriptions can be obtained that depend on the star formation efficiency per cloud free-fall time or cloud lifetime and yield consistency with the “orbital time” empirical relations (McKee & Ostriker 2007). Using global three-dimensional numerical simulations including gas self-gravity, a prescription for star formation, and feedback in the form of thermal energy, Tasker & Bryan (2006) found power-law slopes in $\Sigma_{\text{SFR}} \propto \Sigma^{1+p}$ similar to observed values. Li et al. (2005a, 2006), using smoothed particle hydrodynamics simulations, found both slopes ($p \sim 0.6$) and normalization similar to those in Kennicutt (1998b; $p \approx 0.4$). Their simulations included gravity and sink particles to track the collapsing gas, but did not treat feedback. Recently, Robertson & Kravtsov (2008) performed simulations that included molecular cooling and found that the power-law indices obtained by fitting $\Sigma_{\text{SFR}} \propto \Sigma^{1+p}$ are generally steeper if all of the gas, rather than just molecular gas, is included; this is consistent with recent observational results.

In this work we investigate how SN-driven feedback affects subsequent star formation in gas disks, including star formation rates. We model feedback with a direct momentum input, rather than using a thermal energy input (when underresolved, the latter approach suffers from overcooling and the resulting momentum input is too low). Our work also differs from other recent simulations in our approach to treating disk thickness effects; these can be very important to determining the star formation rate, but direct resolution requiring zones < 5 pc in size can be prohibitively expensive to implement in global disk models.

The evolution of large gas clouds is also relevant to studies of spiral structure. In previous work (Shetty & Ostriker 2006, hereafter Paper I) we simulated global disks with an external spiral potential and found that gravitational instability causes gas in the spiral arms to collapse to form clouds with masses $\sim 10^7 M_{\odot}$, similar to masses of GMAs and H I superclouds. We found that

gas self-gravity is also crucial for the growth of spurs (or feathers), which are interarm features that are connected to the spiral arm clouds (see also Kim & Ostriker 2002). Observations have shown that spurs are indeed ubiquitous in grand-design galaxies and are likely connected with large clouds in the spiral arms (Elmegreen 1980; La Vigne et al. 2006). If grand-design spiral structure is long lasting, as hypothesized by density wave theory (Lin & Shu 1964; Bertin & Lin 1996 and references therein), then feedback mechanisms dispersing the spiral arm clouds must nevertheless leave the global spiral pattern intact. One of the goals of this work is to assess the effect of star formation feedback in massive clouds on the global spiral morphology.

Conversely, the spiral arms also affect the initial formation of clouds, therefore also impacting the star formation process. Observations show that most H α emission in grand-design galaxies occurs downstream from the primary dust lanes. An explanation for these observations is that gas is compressed as it flows through the spiral potential minimum, leading to cloud formation; then at some later time, stars form within these compressed gas clouds. Consensus on the exact nature of spiral arm offsets has not yet been reached, however, owing to both observational limitations and diverse theoretical views on the star formation process. Further, the relative importance of spiral arm triggering is still not completely understood. Vogel et al. (1988) found that the star formation efficiency (in molecular gas) in the spiral arms of the grand-design galaxy M51 is only larger by a factor of a few compared with interarm regions. Other observational studies comparing star formation rates in grand-design spiral galaxies and those without strong spiral structure found similar results (see Knapen et al. 1996; Kennicutt 1998a and references therein). As a result, density waves may primarily gather gas in the spiral arms (enhancing the ability to form GMCs), but may not significantly affect the star formation efficiency within any given molecular parcel. Without a large-scale density wave, a similar fraction of gas might still collapse (per galactic orbit) to form clouds via other mechanisms (including large-scale gravitational instabilities), but not in a coherent fashion. Here, we explore the differences in cloud formation properties in gaseous disks with and without an external spiral driving mechanism.

In this work we are interested in the effect of feedback from star formation in large clouds, such as GMCs and GMAs, on the star formation rate, as well as on the overall dynamics and subsequent cloud formation in galaxy disks. This work extends the models presented in Paper I: numerical hydrodynamic simulations of global disks with gas self-gravity. With the resolutions of our models, massive GMAs do not fragment into smaller GMCs, so significant energy input is required to unbind the gas in these concentrations. If this energy is provided by star formation feedback, multiple massive stars would be needed to destroy the GMAs. In this work we model feedback by considering the impact on large clouds of single energetic events. In practice, this could represent multiple correlated SNe; this can also be considered simply as an expedient but cleanly parameterizable feedback model at one extreme of the range of event correlation.⁴ We then study the resulting nature of the turbulent gaseous disk, as well as the formation and evolution of the clouds that form in the turbulent medium. In § 2 we describe our numerical simulation approach, including model parameters and the feedback algorithm. We then present and analyze our simulation results in § 3. In § 4 we discuss our results in the context of other work and summarize our conclusions.

⁴ In future work we intend to explore how the degree of feedback correlation affects the results.

2. MODELING METHOD

2.1. Basic Hydrodynamic Equations

To study the growth and destruction of clouds in a gaseous disk, we simulate the evolution of the gaseous component by integrating the equations of hydrodynamics. As in Paper I, we include the gravitational potential of the gas. Our models are two-dimensional, except that the vertical structure of the disk is included in the calculation of self-gravity, embodied in a function $f(z)$ (see below and the Appendix). The governing hydrodynamic equations, including self-gravity, are

$$\frac{\partial \Sigma}{\partial t} + \nabla \cdot (\Sigma \mathbf{v}) = 0, \quad (2)$$

$$\frac{\partial \mathbf{v}}{\partial t} + \mathbf{v} \cdot \nabla \mathbf{v} + \frac{1}{\Sigma} \nabla \Pi = -\nabla(\Phi_{\text{ext}} + \Phi) - \frac{v_c^2}{R}, \quad (3)$$

$$\nabla^2 \Phi = 4\pi G f(z) \Sigma. \quad (4)$$

Here, Σ , \mathbf{v} , and Π are the gas surface density, vertically averaged velocity, and vertically integrated pressure, respectively, and v_c is the unperturbed circular orbital velocity. For simplicity, we assume an isothermal equation of state, so that $\Pi = c_s^2 \Sigma$, where c_s is the sound speed. The term Φ is the gaseous self-gravitational potential. To grow gaseous spiral arms, we include an external spiral potential Φ_{ext} to model the perturbation produced by the nonaxisymmetric stellar distribution, which is specified at time t in the inertial frame by

$$\Phi_{\text{ext}}(R, \phi; t) = \Phi_{\text{ext},0} \cos [m\phi - \phi_0(R) - m\Omega_p t], \quad (5)$$

where m , $\phi_0(R)$, and Ω_p are the number of arms, reference phase angle, and spiral pattern speed, respectively. We only consider models with a constant pitch angle i , so that

$$\phi_0(r) = -\frac{m}{\tan i} \ln R + \text{const}. \quad (6)$$

2.2. Model Parameters

Similar to Paper I, the sound speed c_s and rotational velocity v_c are constant in space and time, $c_s = 7 \text{ km s}^{-1}$ and $v_c = 210 \text{ km s}^{-1}$. We adopt the code unit of length $L_0 = 1 \text{ kpc}$. Using c_s as the code unit for velocity, the time unit $t_0 = L_0/c_s = 1.4 \times 10^8 \text{ yr}$, which corresponds to one orbit $t_{\text{orb}} = 2\pi/\Omega_0$ at a fiducial radius $R_0 = L_0 v_c / 2\pi c_s = 4.77 \text{ kpc}$. Our results will scale to other values of R_0 and L_0 with the same ratio, as well as to models with the same ratio $v_c/c_s = 30$.

In Paper I we explored different external spiral potential strengths,

$$F \equiv \frac{\Phi_{\text{ext},0} m}{v_c^2 \tan i}, \quad (7)$$

which is the ratio of the maximum radial perturbation force to the radial force responsible for a constant rotational velocity v_c . We found that spurs form in disks with strong external potential strengths. Since one of our objectives is to assess the evolution of the spurs in disks including feedback, here we only simulate disks with $F = 10\%$, for both two-arm and four-arm spiral galaxies ($m = 2$ and 4). The corotation radius of $25L_0$ corresponds to 25 kpc and a pattern speed of $8.4 \text{ km s}^{-1} \text{ kpc}^{-1}$, for spiral models using our fiducial parameters. We also simulate disks with no external spiral forcing.

In our computation of gas self-gravity, we include the effect of the thickness of the disk via $f(z)$, which also acts as softening. We assume a Gaussian vertical gas distribution, with scale height $H \propto R$, so the disk flares at larger radii (see Appendix). For a given surface density, the effective midplane density is given by $\rho_0 = \Sigma/[H(2\pi)^{1/2}]$. As described in Paper I and Kim & Ostriker (2007), including the effect of thickness provides an important stabilizing effect on the disk. For most of our simulations, we use $H/R = 0.01$.

As in Paper I, the Toomre parameter $Q_0 \equiv \kappa_0 c_s / (\pi G \Sigma_0)$ and the surface density Σ_0 at R_0 are related by

$$\Sigma_0 = \frac{2\sqrt{2}c_s^2}{GL_0 Q_0} = \frac{32}{Q_0} M_\odot \text{ pc}^{-2} \left(\frac{c_s}{7 \text{ km s}^{-1}} \right)^2 \left(\frac{L_0}{\text{kpc}} \right)^{-1}. \quad (8)$$

For flat rotation curves, the epicyclic frequency $\kappa = \sqrt{2}\Omega = \sqrt{2}v_c/R$. Our models initially have $\Sigma \propto R^{-1}$, so that Q is constant for the whole disk.

2.3. Numerical Methods

Since this work is an extension of previous work, we refer the reader to Paper I for a description of the cylindrical-symmetry version of the ZEUS code (Stone & Norman 1992a, 1992b) that we use to carry out our simulations. We use a parallelized version of the hydrodynamic code and gravitational potential solver, allowing us to increase the number of zones in the grid relative to the models of Paper I. For our standard grid we set the azimuthal range to $0-\pi/2$ radians and the radial range to $4-11 \text{ kpc}$. We implement outflow and periodic boundary conditions in the radial and azimuthal directions, respectively. These models have 1024 radial and 1024 azimuthal zones. Since the radial grid spacing is logarithmic, the resolution varies; the linear resolution in each dimension (ΔR , $R\Delta\phi$) varies from $\sim(4 \text{ pc}, 6 \text{ pc})$ in the innermost region to $\sim(11 \text{ pc}, 17 \text{ pc})$ at the outer boundary. These high resolutions allow the Truelove criterion (Truelove et al. 1997) to be satisfied throughout the simulation as gas collapses to form self-gravitating clumps.

In this work we use a different method to compute the gravitational potential from that in Paper I. Here, we use a method derived from that described by Kalnajs (1971) in polar coordinates (see also Binney & Tremaine 1987). This method employs the convolution theorem for a disk decomposed into logarithmic spiral arcs. We implement softening to account for the nonzero thickness of the disk. We describe the method in detail in the Appendix.

We note that for simulations with the standard grid and including a spiral potential, the limit in azimuth requires that $m = 4$ (four arms). However, we also explore some models with $m = 2$ patterns, with the azimuthal range $0-\pi$, using twice as many azimuthal zones as the standard grid so that the physical resolutions of both simulations are equivalent.

2.4. Feedback: Event Description and Algorithm

Equations (2)–(4) only describe the flow as gas responds to self-gravity and to the external spiral perturbation, if one is present. However, those equations do not describe any feedback that would occur after a self-gravitating cloud forms and fragments into smaller scale structures, ultimately forming stars with a range of masses. In the real ISM of galaxies, clouds are dispersed by the combination of photoevaporation by UV radiation from massive stars and the “mechanical” destruction by expanding H II regions and SNe.

We include in our simulations a very simple feedback prescription by implementing “feedback events,” each representing

momentum input from a number of SNe (or, alternatively, multiple overlapping expanding H II regions). The specific SN rate, R_{SN} , averaged over all mass M_{dense} above a chosen threshold density in a galaxy is

$$R_{\text{SN}} = \frac{\text{Number of SNe}}{M_{\text{dense}} \times \text{time}}. \quad (9)$$

When this rate is applied to an individual dense cloud of mass M_{cl} with a lifetime t_{cl} , the average number of SNe in the cloud will be

$$N_{\text{SN}} = R_{\text{SN}} M_{\text{cl}} t_{\text{cl}}. \quad (10)$$

If the total mass of stars of all masses formed per single SN is M_{SN} and the star formation efficiency over a cloud lifetime is ϵ_{SF} , then

$$N_{\text{SN}} = \epsilon_{\text{SF}} \frac{M_{\text{cl}}}{M_{\text{SN}}}. \quad (11)$$

Equating expressions (10) and (11), the mean cloud lifetime is

$$t_{\text{cl}} = \frac{\epsilon_{\text{SF}}}{R_{\text{SN}} M_{\text{SN}}}. \quad (12)$$

In a given time interval δt , such as the time between successive computations in the numerical evolution, the probability P that a cloud (of mean lifetime t_{cl}) is destroyed is $\delta t/t_{\text{cl}}$. Thus,

$$P = \delta t R_{\text{SN}} M_{\text{SN}} / \epsilon_{\text{SF}}. \quad (13)$$

In our algorithm, clouds are defined as regions with densities above a chosen threshold. If a particular zone is a local density maximum, that zone is selected as the center of the feedback event. For any such identified cloud, a star formation event is initiated with a probability per time step given by equation (13). In each cloud that is determined to undergo feedback, gas is evenly spread out in a circular region with a prescribed bounding radius. Gas in each zone in the circular region is assigned an outward velocity (relative to the center) to expand the feedback “bubble.” A constant azimuthal velocity is also added such that total galactocentric angular momentum is conserved. The velocity profile inside the bubble is proportional to the distance from the bubble center. For most of our simulations, we choose the radius of the feedback bubble to be 75 pc, which corresponds to 12–23 pixels, depending on the radial location. In this way, the initially collapsing cloud gas is forced back into the surrounding ISM.

In our simulation we only consider the isothermal expansion of the clouds, since we assume an isothermal equation of state. Thus, we can only consider the net energy input at a stage when expansion of the shell has become strongly radiative. Numerical simulations show that for a single SN of energy $E_{\text{SN}} \approx 10^{51}$ ergs, the radial momentum during the radiative stage is $P_{\text{rad}} \approx (3-5) \times 10^5 M_{\odot} \text{ km s}^{-1}$ (Chevalier 1974; Cioffi et al. 1988). During the subsequent evolution of the bubble, the shell momentum P_{sh} is conserved and is equal to P_{rad} . Wind-driven and pressure-driven H II region bubbles similarly are accelerated to reach a final momentum P_{rad} .

For a total number of massive stars formed given by equation (11) and assuming correlation in time, the total momentum applied to the shell is

$$P_{\text{sh}} = N_{\text{SN}} P_{\text{rad}} = \epsilon_{\text{SF}} \frac{M_{\text{cl}}}{M_{\text{SN}}} P_{\text{rad}}. \quad (14)$$

TABLE 1
PARAMETERS FOR STANDARD^a MODELS

Model	Q_0	m	R_{SN}^b	ϵ_{SF}	$P_{\text{rad}} (10^5 M_{\odot} \text{ km s}^{-1})$
(1)	(2)	(3)	(4)	(5)	(6)
Q1A.....	1	0	1	0.025	0.34
Q1B.....	1	0	1	0.05	0.34
Q1D.....	1	0	10	0.05	3.4
Q1SA.....	1	4	1	0.025	0.34
Q1SB.....	1	4	1	0.05	0.34
Q1SC.....	1	4	1	0.05	3.4
Q1SD.....	1	4	10	0.05	3.4
Q1SE.....	1	4	10	0.05	0.34
Q2SA.....	2	4	1	0.025	0.34
Q2SB.....	2	4	1	0.05	0.34
Q2SC.....	2	4	1	0.05	3.4
Q2SD.....	2	4	10	0.05	3.4

^a By standard we mean 1024×1024 zones, $R \in [4, 11]$ kpc, and $\phi \in [0, \pi/2]$ radians.

^b This is in units of $2 \times 10^{-11} M_{\odot}^{-1} \text{ yr}^{-1}$, i.e., number of SNe per 50 yr per $10^9 M_{\odot}$.

The shell velocity V_{sh} is

$$V_{\text{sh}} = \frac{P_{\text{sh}}}{M_{\text{sh}}} = \epsilon_{\text{SF}} \frac{M_{\text{cl}}}{M_{\text{sh}}} \frac{P_{\text{rad}}}{M_{\text{SN}}}. \quad (15)$$

Here, M_{sh} is the sum of M_{cl} and any ambient gas in the (circular) feedback region. Assuming $M_{\text{SN}} = 100 M_{\odot}$ and $\epsilon_{\text{SF}} = 0.05$, for $P_{\text{rad}} = 3 \times 10^5 M_{\odot} \text{ km s}^{-1}$, $V_{\text{sh}} = (150 \text{ km s}^{-1})(M_{\text{cl}}/M_{\text{sh}})$.

Given our feedback prescription, the two key parameters are the probability per unit time for cloud destruction (eq. [13]) and the momentum input in the feedback event (eq. [14]). For the simulations presented here, we explore a range in the rate R_{SN} and in the momentum input per massive star, P_{rad} . The specific SN rate is set either to $R_{\text{SN}} = [(10^9 M_{\odot})(50 \text{ yr})]^{-1} = 2 \times 10^{-11} M_{\odot}^{-1} \text{ yr}^{-1}$ (comparable to that in the Milky Way) or 10 times that rate (these models are denoted by $R_{\text{SN}} = 1$ or 10 in Table 1). Since $M_{\text{SN}}/\epsilon_{\text{SF}}$ in equation (13) appears as its inverse in equation (14), we fix $M_{\text{SN}} = 100 M_{\odot}$ for all simulations, motivated by the initial mass function of Kroupa (2001), and explore variations in ϵ_{SF} . Scaling to fiducial values, we then have

$$t_{\text{cl}} = 2.5 \times 10^7 \text{ yr} \left(\frac{\epsilon_{\text{SF}}}{0.05} \right) \left(\frac{R_{\text{SN}}}{2 \times 10^{-11} M_{\odot}^{-1} \text{ yr}^{-1}} \right)^{-1} \quad (16)$$

for the typical lifetime of dense clouds. The momentum P_{rad} is set either to 3.4×10^4 or $3.4 \times 10^5 M_{\odot} \text{ km s}^{-1}$, in order to allow for a range in feedback energy and out-of-plane losses (venting from the galaxy) that reduce P_{rad} for a given energy input.

We note that for low values of P_{rad} , the energy input will not be sufficient to destroy a dense, bound cloud. In particular, a cloud of surface density Σ_{cl} will become unbound only if $V_{\text{sh}} \gtrsim (2G)^{1/2} (\pi \Sigma_{\text{cl}} M_{\text{cl}})^{1/4}$. For $\Sigma_{\text{cl}} = 200 M_{\odot} \text{ pc}^{-2}$ and $M_{\text{cl}} = 10^6 M_{\odot}$, the minimum shell velocity is $\sim 15 \text{ km s}^{-1}$. For our larger value of P_{rad} , this inequality is comfortably satisfied, but for the smaller value it is not. We indeed find that for the low- P_{rad} models, clouds are not destroyed by feedback. For these models, then, the ratio $t_{\text{cl}} \equiv \epsilon_{\text{SF}}/(R_{\text{SN}} M_{\text{SN}})$ becomes the mean interval between (non-destructive) feedback events in a given cloud.

Before any feedback, the spiral models are executed for some time to allow gas to concentrate (due to self-gravity) and form clouds in spiral arms. In simulations without spiral forcing, condensations begin to grow due to an initial 0.1% density perturbation. As a result of shear, the first structures that form are

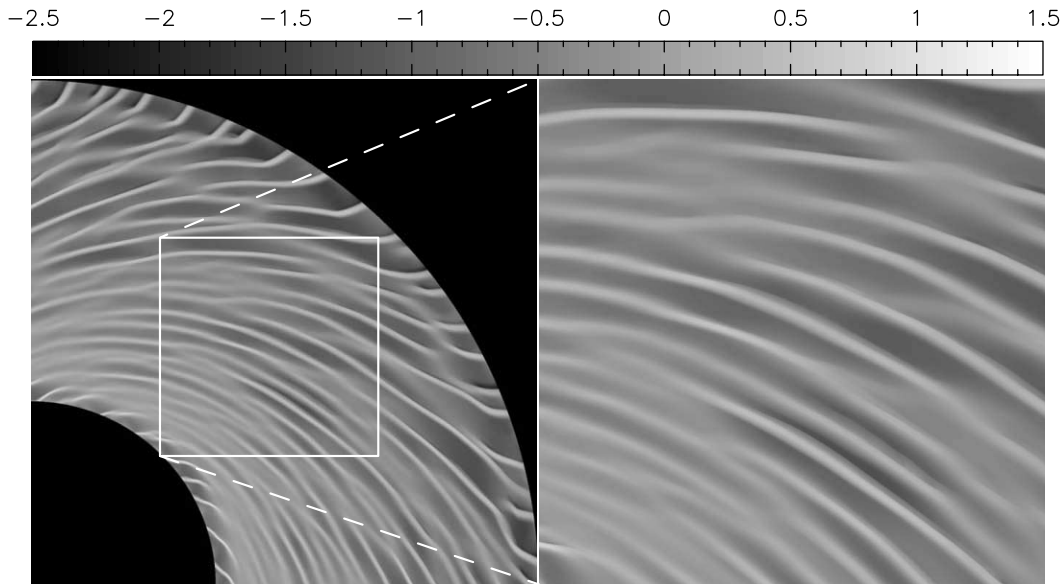


FIG. 1.—Density snapshots of $Q_0 = 1$ nonspiral model before any feedback, at time $t/t_{\text{orb}} = 0.84$. Gray scale is in units of $\log(\Sigma/\Sigma_0)$. [See the electronic edition of the *Journal* for a color version of this figure.]

large-scale flocculent spiral-like features, which we termed “sheared background features” in Paper I. Gas in these features then collapses to form distinct clouds. Thus, we wait until some threshold density is reached before feedback occurs. For most models, the threshold density is $\Sigma/\Sigma_0 = 10$ (this sets the threshold Σ at $320 M_\odot \text{ pc}^{-2}$ for $Q_0 = 1$, and $160 M_\odot \text{ pc}^{-2}$ for $Q_0 = 2$). We hereafter refer to any contiguous structure in our simulation with a density above this chosen threshold as a “cloud,” regardless of whether the given structure hosts a feedback event or not.

We note that with our feedback prescription, the star formation rate is given by the mass in dense gas (i.e., exceeding the threshold surface density) times $R_{\text{SN}}M_{\text{SN}}$. This linear relation is supported by the shallow slopes of Σ_{SFR} versus Σ_{mol} (as observed in CO emission). In some other recent work (e.g., Li et al. 2005a, 2006; Tasker & Bryan 2006, 2008; Robertson & Kravtsov 2008), the star formation rate is taken as equal to the mass (with density above some threshold) divided by the free-fall time at that density, times some efficiency factor. Our prescription is therefore equivalent to choosing a ratio of efficiency over free-fall time at the surface density threshold of $\epsilon_{\text{ff}}/t_{\text{ff}} = R_{\text{SN}}M_{\text{SN}} = (5 \times 10^7 - 5 \times 10^8 \text{ yr})^{-1}$. Since the mean internal density within real GMCs (which have surface densities similar to our critical threshold) is $\sim 100 \text{ cm}^{-3}$, with corresponding free-fall time of 4 Myr, our models would cover a range of star formation efficiencies per free-fall time of $\epsilon_{\text{ff}} \sim 1\% - 10\%$.

3. SIMULATION RESULTS

We first present simulations with standard grid parameters, without spiral structure. We then show the results of simulations including spiral structure, as well as simulations pertaining to different radial regions.

Table 1 shows the initial conditions of the standard set of models we present, as well as the relevant parameters controlling the feedback events. Column (1) lists each model. Column (2) shows the initial Toomre Q parameter which is initially constant for the whole disk. Column (3) indicates the number of arms, all with $F = 10\%$. Column (4) gives the SN rate, which is required for setting the probability that a feedback event occurs in a cloud (see eq. [13]). Column (5) shows the assumed star formation

efficiency, and column (6) gives the adopted momentum input per massive star. For these models $H/R = 0.01$.

3.1. Disks without Spiral Structure

Figure 1 shows a snapshot of the model with $Q_0 = 1$, at time $t/t_{\text{orb}} = 0.84$, without an external spiral potential and before any feedback. As discussed in § 2.4, trailing features grow due to the self-gravity and shear in the disk (see Paper I for details). The most dense structures grow as sheared, trailing features. It is in these regions where the first SN will occur to disperse the dense gas.

Figure 2 shows a snapshot of model Q1A, at time $t/t_{\text{orb}} = 1.125$. For model Q1A, the SN parameters are all at the low end of the range. At the time of this snapshot, 105 feedback events have occurred, in clouds which have mean $M_{\text{cl}} = 1.2 \times 10^6 M_\odot$. The main difference between Figures 2 and 1 is the shape of the trailing features. The feedback events have caused the features to become fragmented at some locations. However, dispersal of gas due to feedback was not sufficient to prevent or reverse the inflow of gas into the high-density agglomerations. Either the SNe do not occur rapidly enough or do not have enough momentum to alter the basic morphology. Even increasing both the SN rate by a factor of 10 and doubling the star formation efficiency makes little difference; the strong self-gravitational force from the trailing features keeps much of the gas in those structures. Increasing the SN momentum (or equivalently the velocity) by up to a factor of 8 still does not significantly affect the outcome; much of the gas is contained in the sheared structures at any given time.

It is only when P_{rad} is increased to $3.4 \times 10^5 M_\odot \text{ km s}^{-1}$, along with increasing R_{SN} by a factor of 10 and ϵ_{SF} to 0.05, that we find a significant difference compared to the case Q1A, as in model Q1D shown in Figure 3. The velocity is sufficiently large to drive gas away from the density maxima of the trailing structures. Further, the rate is high enough that a large number of events occur to significantly alter the morphology, in comparison with Figure 2. Feedback events in this model are so frequent and energetic that collisions between bubbles occur. In some instances, such collisions create density enhancements that later result in more collapse and subsequent feedback along the bubble interface. At time $t/t_{\text{orb}} = 1.125$ (Fig. 3a), we can still make out the underlying loci

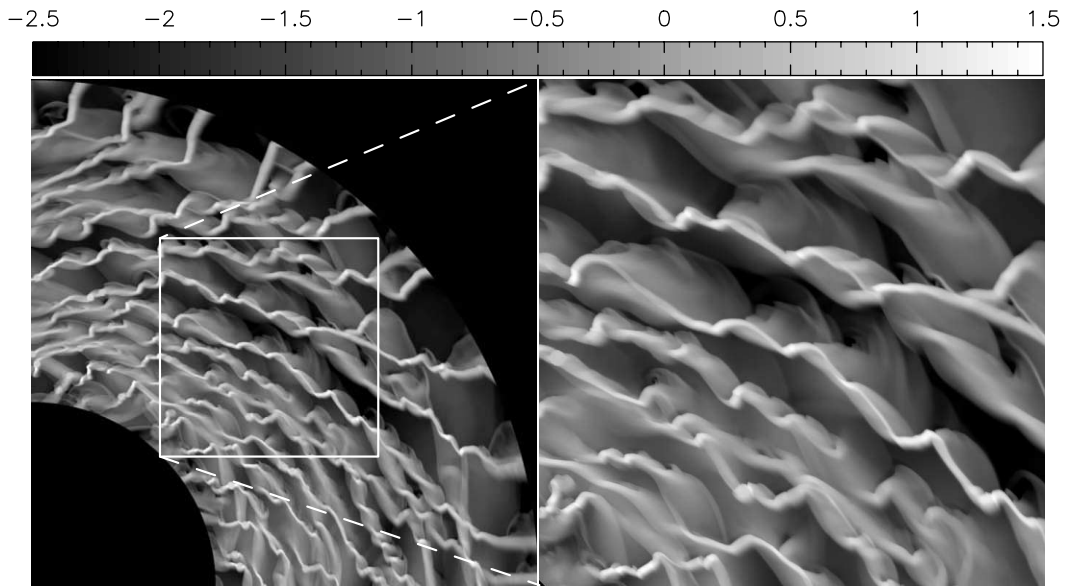


FIG. 2.—Density snapshots of model Q1A, at time $t/t_{\text{orb}} = 1.125$. Gray scale is in units of $\log(\Sigma/\Sigma_0)$. [See the electronic edition of the Journal for a color version of this figure.]

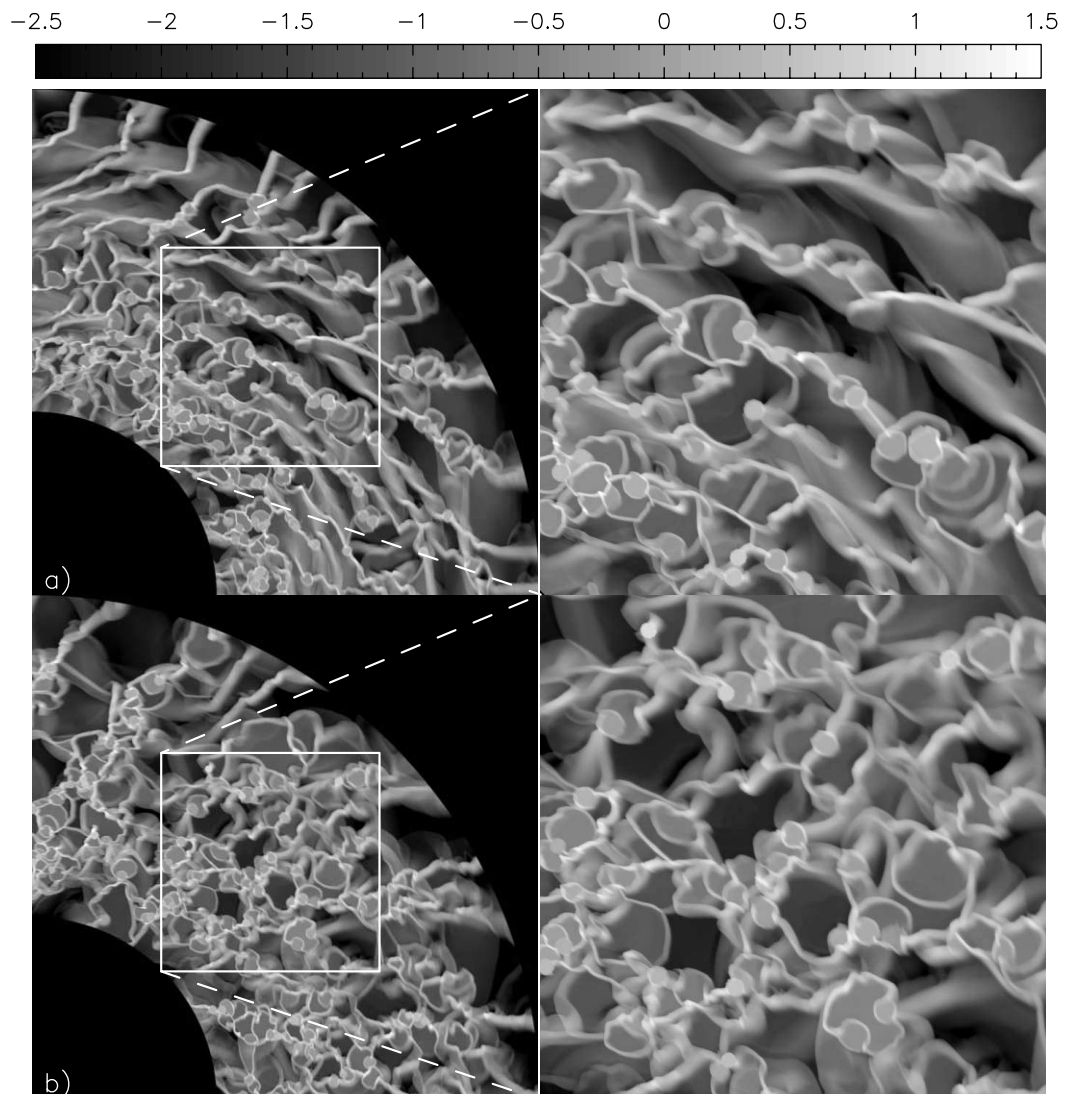


FIG. 3.—Density snapshots of model Q1D, at time (a) $t/t_{\text{orb}} = 1.125$ and (b) 1.375. Gray scale is in units of $\log(\Sigma/\Sigma_0)$. [See the electronic edition of the Journal for a color version of this figure.]

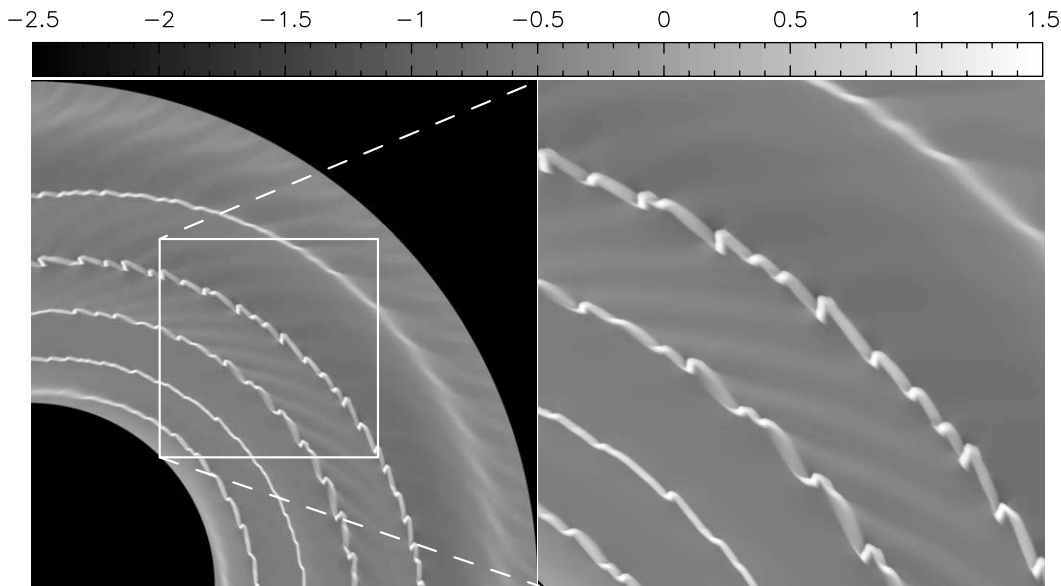


FIG. 4.—Density snapshots of $Q_0 = 1$ spiral model, without feedback, at $t/t_{\text{orb}} = 0.675$. Gray scale is in units of $\log(\Sigma/\Sigma_0)$. [See the electronic edition of the Journal for a color version of this figure.]

of the initial structures formed by gravitational instability and shear, although 537 feedback events have occurred up to this time. Yet, after an additional 26 Myr and 75 feedback events (Fig. 3b), the dominant large-scale features do not have a single pitch angle. Further, the locations of many of the bubbles are clustered. Although gas is driven away from the initial structures formed before feedback, at later times clouds form in clusters near the initial density maxima and where feedback bubbles overlap. Qualitatively, the features in the disk, consisting of filaments and bubbles, are similar to the global models including feedback of Wada & Norman (2001). We discuss the masses of the clouds in both “nonspiral” and spiral models in § 3.2.

In disks with $Q_0 = 2$, sheared features will also grow, but need more time to develop than in the $Q_0 = 1$ disks. Because of its relative stability, after $t/t_{\text{orb}} = 2$ only a few clouds have formed. As a result, implementing feedback does not affect the majority of the disk. To study the effect of feedback in $Q_0 = 2$ disks, another mechanism is necessary to grow clouds everywhere in the disk. We thus simulate $Q_0 = 2$ disks with an external spiral potential and then implement feedback to destroy the spiral arm clouds that grow.

3.2. Disks with Spiral Structure

In disks with spiral structure, the stellar spiral potential acts as a source of perturbation; the compression of gas as it flows through the potential eventually leads to the growth of self-gravitating clouds. We explore the effect of feedback on the morphology of the gaseous spiral arms and interarm spurs, as well as any subsequent cloud formation.

Figures 4 and 5 show snapshots of models with $m = 4$, for $Q_0 = 1$ and 2, without any feedback. In the spiral models, the growth of spiral arm clouds occurs sooner than the growth of clouds formed by natural instabilities in a rotating self-gravitating disk.⁵ Figures 4 and 5 show snapshots of models without any feedback, although in the $Q = 1$ snapshot (Fig. 4) the densities

⁵ In our models, the amplitude of the spiral perturbation is “turned on” gradually, reaching the maximum amplitude F at $t/t_{\text{orb}} = 1$. Because of this imposed “turn-on” time, the growth rate of GMCs in our models is not representative of actual GMC formation timescales.

have surpassed the threshold density $\Sigma/\Sigma_0 = 10$ chosen for models with feedback. Note that while the $Q = 1$ model (with strong self-gravity) shows dense gas knots within the arm, the $Q = 2$ model (with weaker self-gravity) shows spurlike features; gas does not collapse as promptly.

For both models Q1SA and Q2SA, the SN momenta are insufficient to offset the growth of clouds and spurs resulting from the spiral potential. After a feedback event, the dispersed cloud gas flows back toward the spiral arm. As a result, clouds continue to grow over time. Further, the spurs also continue to grow in density. Without feedback, self-gravitating spiral arm clouds cause the surrounding gas to flow in with large velocities. Eventually, the simulations have to be stopped because the Courant time is too small. The time when the simulation ceases, depending partly on our choice of the minimum acceptable Courant time, also depends on which clouds are (randomly) selected for feedback; clouds that have produced large inflow velocities would have to be dispersed for the simulation to continue to evolve.

We again find that large SN momenta are required to sufficiently disperse clouds so that immediate recollapse does not occur. For such models, the SN rate has an effect on the number of subsequent clumps formed. Figure 6 shows a snapshot of models Q1SC and Q1SD, ~ 21 Myr after the first feedback events. At this time, 53 feedback events have occurred in model Q1SC and 540 in model Q1SD. In model Q1SC, it is clear that most, if not all, feedback events originated in the spiral arms. However, in model Q1SD, many feedback events have occurred in interarm regions. The spiral arms are not as identifiable, although at this time the remnants of spurs are still identifiable. Further, model Q1SD contains many more clumps than model Q1SC. The enhanced SN rate has caused the collision of more shell remnants, which lead to the formation of self-gravitating clumps at the interfaces. In both cases, feedback events have caused gas to be dispersed from the arms, eventually removing any trace of the underlying spiral potential, as can be seen in Figure 7.

Figure 8 shows the histogram of the masses of the clouds M_{cl} that hosted feedback events⁶ in models Q1A, Q1D, Q1SA, and

⁶ From eq. (11), feedback events in model Q1A and Q1D on average consist of 300 and 350 SNe, respectively.

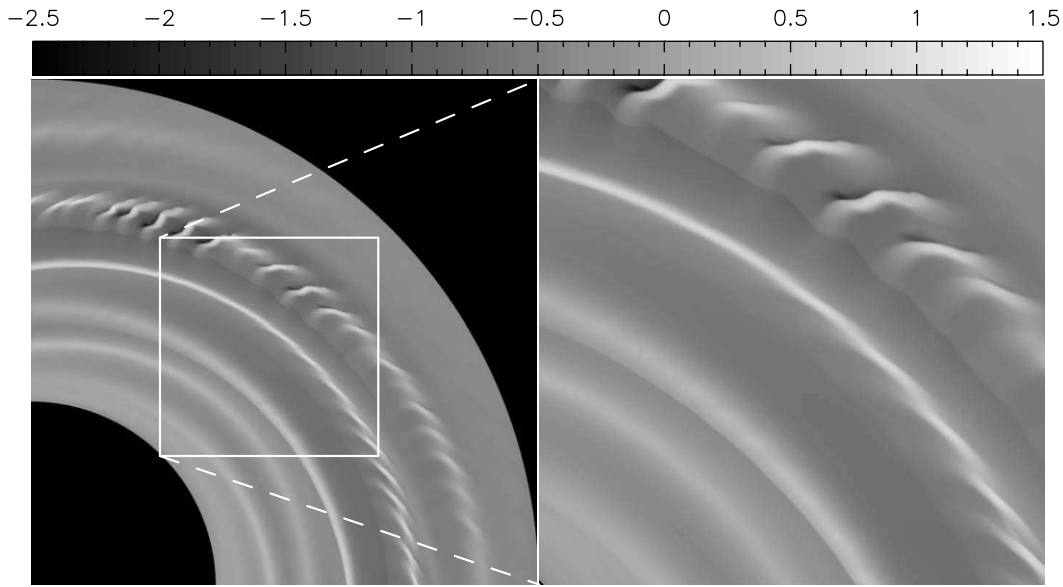


FIG. 5.—Density snapshots of $Q_0 = 2$ spiral model, without feedback, at $t/t_{\text{orb}} = 1.04$. Gray scale is in units of $\log(\Sigma/\Sigma_0)$. [See the electronic edition of the Journal for a color version of this figure.]

Q1SD. In all cases, the maximum mass of the clouds is below $10^7 M_\odot$, and the means and medians for the distributions lie in the range $(0.5\text{--}2.2) \times 10^6 M_\odot$. In model Q1A, most feedback events have occurred in the large-scale sheared features that grow due to gravitational instability. However, in model Q1D, some fraction of the feedback events have occurred in regions of colliding flows. The histogram suggests that clouds formed by colliding flows have characteristically lower masses than those formed in the large-scale sheared features. Similarly, in model Q1SA, most

feedback events have occurred in the spiral arms, since most clouds form in the arms. On average, the clouds in model Q1SD have lower masses, with many clouds formed due to colliding flows initiated in earlier feedback events. For a power law in the mass distribution, $dN/d \log M \propto M^{-\alpha}$, the distribution in the high-end masses for model Q1SD (below the cutoff at $\log M = 6.4$) gives $\alpha \sim 0.6$. This slope and the upper limit in cloud masses is similar to the range and the upper limit in the observed masses of GMCs (see McKee & Ostriker 2007 and references therein).

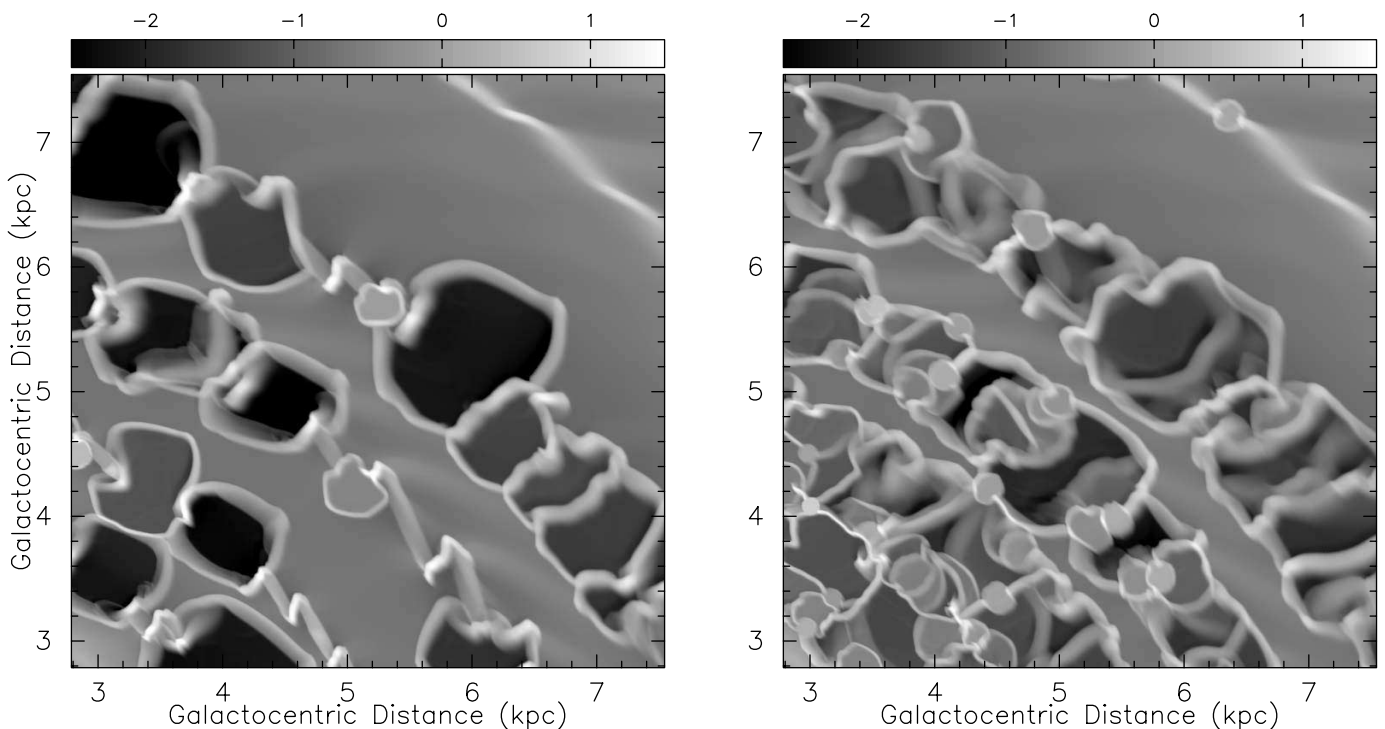


FIG. 6.—Models Q1SC (left) and Q1SD (right) at $t/t_{\text{orb}} = 0.73$. Gray scales are in units of $\log(\Sigma/\Sigma_0)$. [See the electronic edition of the Journal for a color version of this figure.]

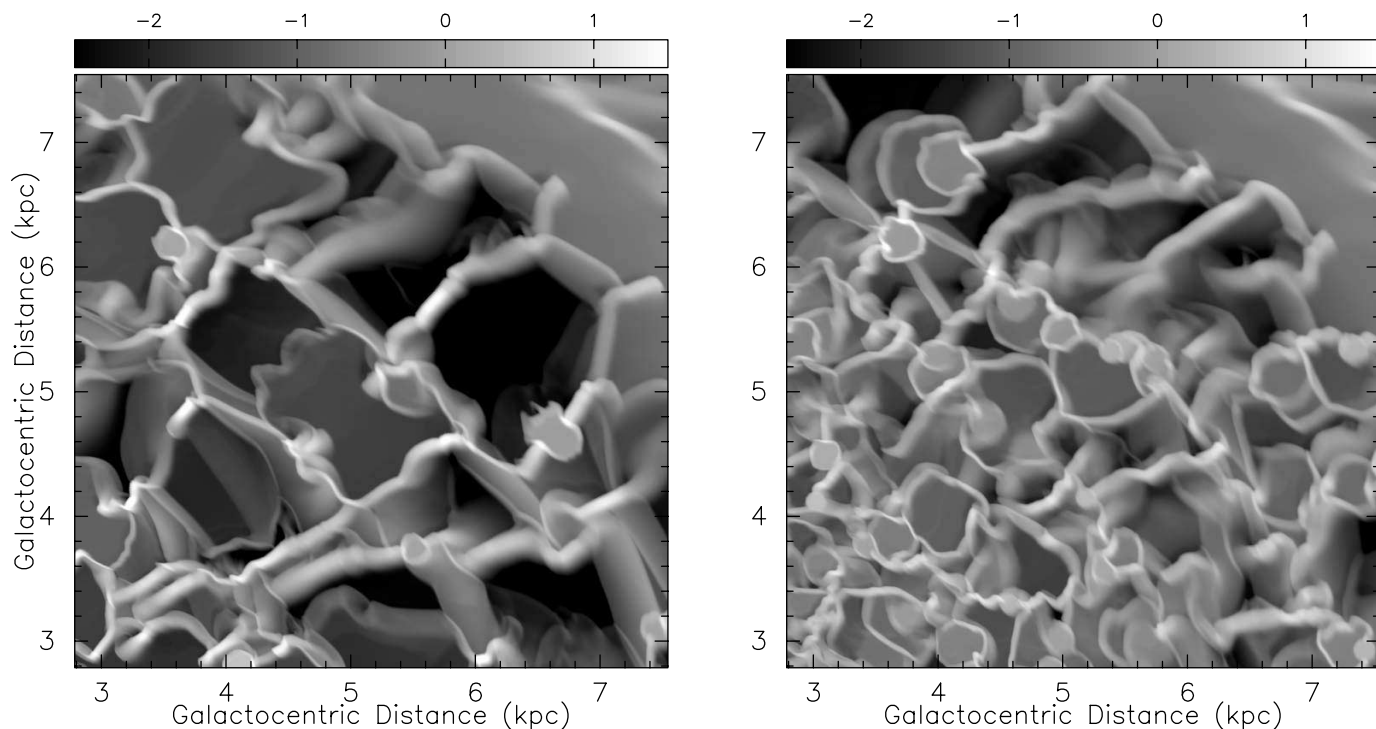


Fig. 7.—Models Q1SC (*left*) and Q1SD (*right*) at $t/t_{\text{orb}} = 1.15$. Gray scales are in units of $\log(\Sigma/\Sigma_0)$. [See the electronic edition of the *Journal* for a color version of this figure.]

A histogram of the masses of all clouds at any given time, scaled by a factor equal to the total duration divided by t_{cl} , reproduces the overall shape of the histogram of the masses of clouds with feedback. A detailed analysis of the cloud mass distribution is not appropriate here, because many of the lower mass clouds are not well resolved and because higher mass clouds would be subject to turbulent fragmentation that we cannot follow. Higher resolution simulations are therefore required to obtain more complete cloud mass

distributions. Nevertheless, it is clear that the upper mass limits for clouds in all models are similar to those in real spiral galaxies.

3.3. Star Formation Properties

3.3.1. Star Formation Rates and Turbulence

For comparison to observations, two quantities of interest are the star formation rate SFR and the turbulent velocity v_{turb} . In

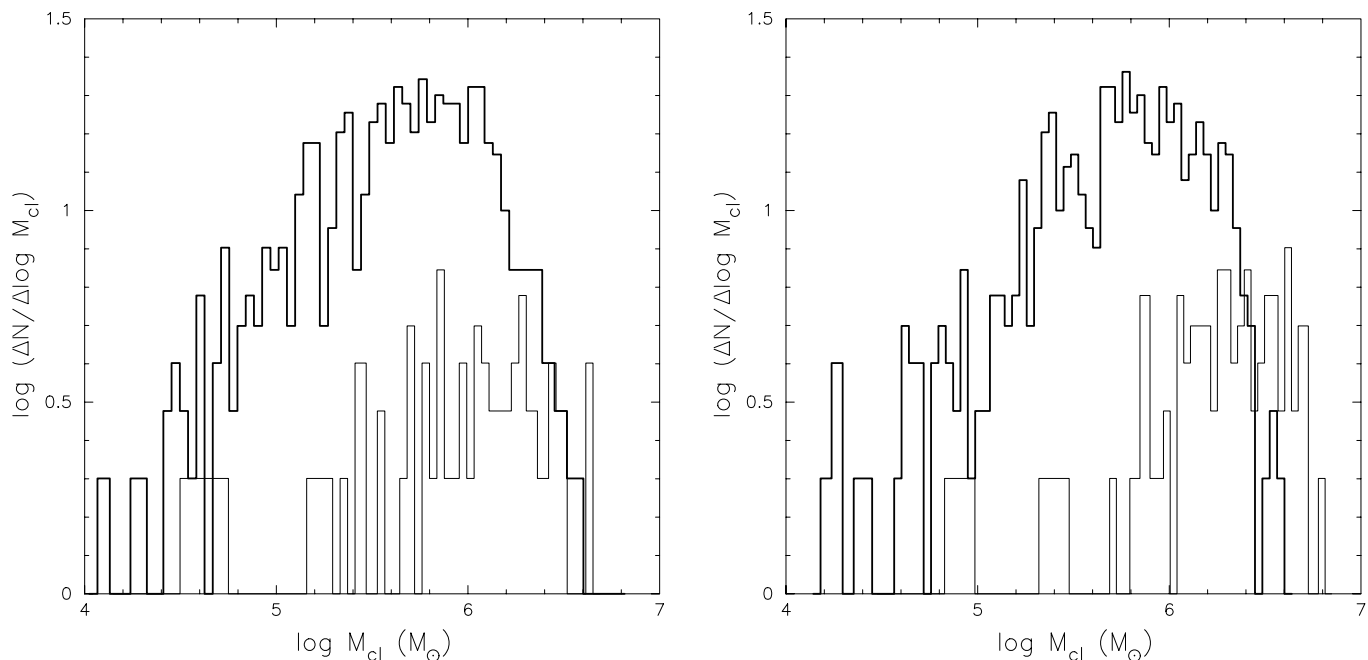


Fig. 8.—Cloud masses in models with strong (*thick lines*) and weak (*thin lines*) feedback. *Left*: Histogram of M_{cl} in models Q1D (*thick histogram*) and Q1A (*thin histogram*), up until time $t/t_{\text{orb}} = 1.125$ (see Figs. 2 and 3). The mean (median) M_{cl} for models Q1A and Q1D are 1.2×10^6 (0.8×10^6) and 0.7×10^6 (0.5×10^6) M_{\odot} , respectively. *Right*: Histogram of M_{cl} in models Q1SD (*thick histogram*) and Q1SA (*thin histogram*), up until time $t/t_{\text{orb}} = 0.73$ (model Q1SD is shown in Fig. 6). The mean (median) M_{cl} for models Q1SA and Q1SD are 2.2×10^6 (1.9×10^6) and 0.8×10^6 (0.6×10^6) M_{\odot} , respectively.

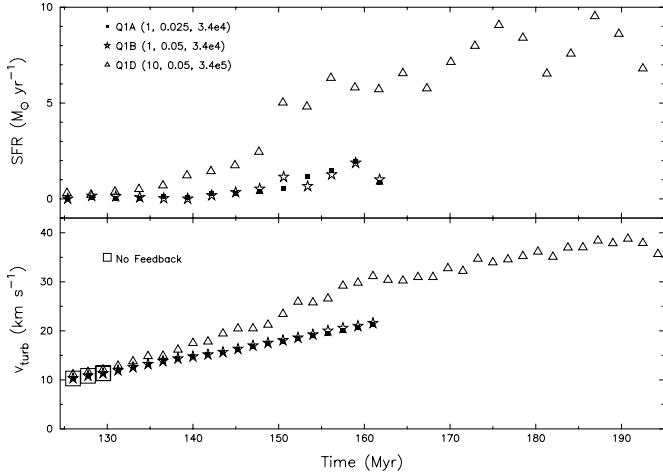


FIG. 9.—SFR (*top*) and v_{turb} (*bottom*) for models with $Q_0 = 1$, without spiral structure. The values in parentheses in the legend are the SN rate parameter R_{SN} , the star formation efficiency ϵ_{SF} , and SN momentum P_{rad} (in $M_{\odot} \text{ km s}^{-1}$) of each model. The large open squares in the bottom panel are the turbulent velocities for a simulation without any feedback.

each simulation, we record each feedback event to determine the SFR. For some chosen time bin Δt , we compute

$$\text{SFR} = \epsilon_{\text{SF}} \frac{\sum M_{\text{cl}}}{\Delta t}, \quad (17)$$

where $\sum M_{\text{cl}}$ is the total mass of all gas in clumps (i.e., above the chosen threshold surface density) that have undergone feedback events in the chosen time interval. (Recall that the mean lifetime of clouds, or the mean interval between star formation events if they are nondestructive, is given by eq. [12].)

We define the turbulent velocity as the rms sum of any non-circular velocities, weighted by the corresponding mass,

$$v_{\text{turb}} = \left[\frac{\sum (\delta v_{i,j})^2 \Sigma_{i,j} A_{i,j}}{\sum \Sigma_{i,j} A_{i,j}} \right]^{1/2}, \quad (18)$$

where $A_{i,j}$ is the area of each zone and only noncircular velocity components are considered, $\delta \mathbf{v} = \mathbf{v} - v_c \hat{\phi}$. Figure 9 shows the star formation rate and turbulent velocity as a function of time, for the $Q_0 = 1$ models without spiral structure. The time bin Δt for our SFR calculation is 3 Myr. In these models, the first feedback events occur at time ~ 125 Myr. However, for the first ~ 25 Myr after feedback begins, the SFR for all models is only a few $M_{\odot} \text{ yr}^{-1}$. Only ~ 25 Myr after the first feedback events does the SFR substantially increase, owing to “propagating” star formation. Further, the Q1D model with large feedback momenta ($P_{\text{rad}} = 3.4 \times 10^5 M_{\odot} \text{ km s}^{-1}$) and a large SN rate ($R_{\text{SN}} = 10$) has the SFR increase to $\sim 10 M_{\odot} \text{ yr}^{-1}$. This occurs because with large velocities and a high global rate, adjacent shells collide and more clouds are formed in the interfaces, which may subsequently undergo star formation.

The bottom panel of Figure 9 shows v_{turb} , for all feedback models without spiral structure, together with results from a simulation without any feedback. For the latter case, we just allow self-gravity to grow clouds indefinitely. When we compute v_{turb} in the model without feedback considering only the low-density gas, we obtain similar values. This suggests that, before any feedback, large-scale motions from disk self-gravity and shear are the primary sources of turbulence (see Kim & Ostriker 2007). The models with low feedback momentum continue the trend of v_{turb}

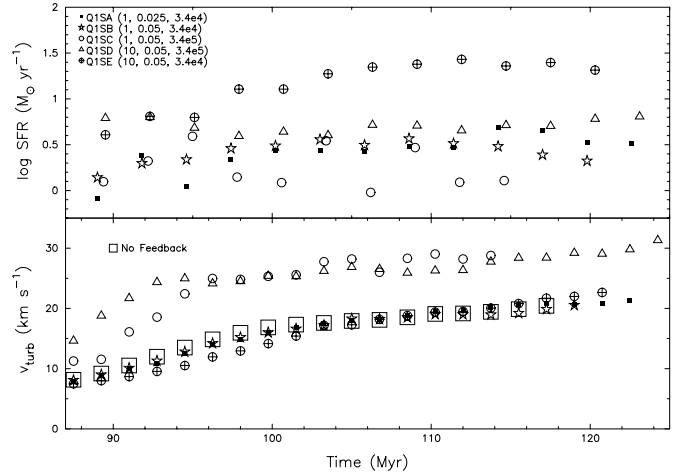


FIG. 10.—Same as Fig. 9, but with spiral structure.

established by the no-feedback case. In a few instances of enhanced feedback, there is a corresponding jump in v_{turb} . The enhanced SFR at later times for the model with large SN momenta also increases levels of v_{turb} .

Figures 10 and 11 show the SFR and v_{turb} for the spiral models with $Q_0 = 1$ and 2. Comparing Figures 10 (with spiral structure) and 9 (without spiral structure), the star formation rate is consistent to within a factor of 2, although slightly larger in some of the spiral models. The general trends from the models without spiral structure are reproduced in Figures 10 and 11. Earlier times are shown in Figure 10, since the spiral arms cause gas to collapse into clouds sooner. It is clear that only in models with large SN shell velocities—and regardless of the input rate R_{SN} —do the turbulent velocities increase appreciably; otherwise, the turbulent velocity (as we have defined it) is dominated by effects from gas self-gravity.

It is interesting to compare results from pairs of models in which one parameter is varied and the others are controlled. Comparing models Q1SE and Q1SB, both have the same $\epsilon_{\text{SF}} = 0.05$ and $P_{\text{rad}} = 3.4 \times 10^4 M_{\odot} \text{ km s}^{-1}$, but the former has R_{SN} larger by a factor 10. The measured SFR in Q1SE is a factor ~ 10 larger than that in Q1SB, consistent with the naive expectation that $\text{SFR} \propto R_{\text{SN}}$. However, when we compare Q1SD with Q1SC, which again differ in R_{SN} by a factor 10, we find SFR ratios differing only by a factor ~ 4 . This same trend is also true for models Q2SD and Q2SC. The reason for this difference in dependence on

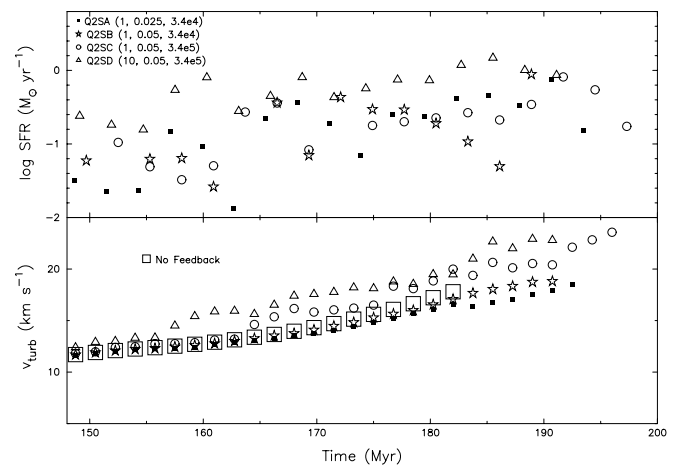


FIG. 11.—Same as Fig. 10, but for models with $Q_0 = 2$.

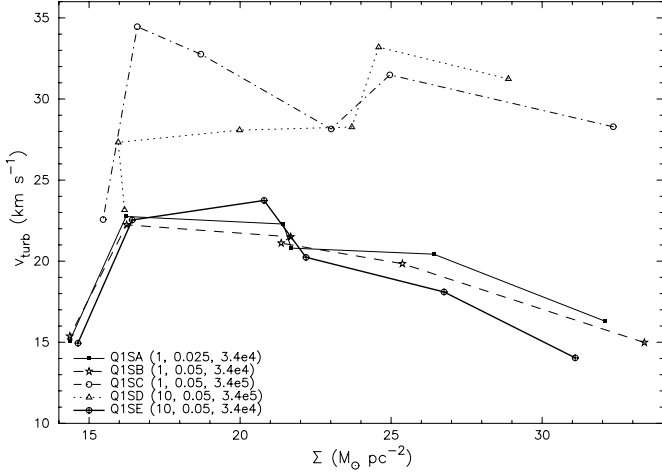


FIG. 12.— Mass-weighted turbulent velocities vs. mean surface density of Q1S models, averaged in annuli of widths 1 kpc, and in the time interval $t/t_{\text{orb}} \in [100, 116]$ Myr. Turbulent velocities are only shown from annuli and time intervals within which feedback events have occurred.

R_{SN} is that the E and B models have low P_{rad} and low turbulence levels, whereas the C and D models have higher P_{rad} and turbulence. Thus, stronger feedback causes the scaling of SFR to depart from $\text{SFR} \propto R_{\text{SN}}$. We note that since $\text{SFR} = R_{\text{SN}} M_{\text{SN}} M_{\text{dense}}$ by definition, the ratios of specific SFRs between any two models differ by their ratios of $R_{\text{SN}} M_{\text{dense}}/M_{\text{tot}}$. Thus, if SFR increases at a rate less than $\propto R_{\text{SN}}$, it implies that increasing R_{SN} decreases the dense gas fraction $M_{\text{dense}}/M_{\text{tot}}$.

We can directly investigate the effect of turbulence by comparing the pair Q1SB and Q1SC, which have the same $\epsilon_{\text{SF}} = 0.05$ and R_{SN} , but momentum input parameters differing by a factor 10. As noted above, this increases the turbulence level in Q1SC compared to Q1SB by about 10 km s^{-1} . It also reduces the SFR in Q1SC compared to Q1SB, by a factor ~ 2 –4. Similarly, Q1SE has lower P_{rad} than Q1SD and a substantially lower turbulence level. For this pair, too, the SFR in the lower turbulence model is higher by a factor ~ 3 –5. As discussed in § 1, in principle turbulence could both enhance star formation (by creating more dense gas in compressions) and suppress star formation (by destroying overdense structures with rarefactions and shear flows). Examining the evolution of Q1SE indeed shows that feedback events only slightly expand clouds, and collapse subsequently resumes. On the other hand, clouds in model Q1SD are completely destroyed after a single feedback event. Evidently, in the models with strong feedback-driven turbulence, the rate of new cloud formation from shell collisions does not compensate for the truncation of star formation when a given cloud is destroyed.

The comparisons of Q1SB to Q1SC and Q1SE to Q1SD indicate that *in net*, the increase of turbulence reduces star formation.⁷ Since the specific SFR is proportional to the dense gas fraction if R_{SN} is held fixed, these results imply that the dense gas mass fraction is lower when the turbulence level is higher.

We show the relationship between the mass-weighted turbulent velocity and the surface density in Figure 12. Most feedback events occur in high-density regions. In the higher density regions, the difference in turbulent velocities (or the velocity dispersions) between models with $P_{\text{rad}} = 3.4 \times 10^4$ and $3.4 \times 10^5 M_{\odot} \text{ km s}^{-1}$ is $\geq 7 \text{ km s}^{-1}$. At lower density regions, where there have been fewer feedback events, the dispersions of all models are comparable.

⁷ We note that models Q2SB and Q2SC also show the same generic behavior, but with a smaller difference in the turbulence level; the suppression of star formation is also lesser.

Figure 13 shows the turbulent power spectrum (power $\propto v^2$) of model Q1D. The power is shown at constant wavenumbers k_R and k_{ϕ} . The slopes of the power spectra range from -2.5 to -3 . For models that evolve for significant amounts of time, such as model Q1D, the power spectra are relatively independent of time. These results are consistent with turbulence dominated by numerous shocks, or Burgers turbulence. From Figure 13, the amplitudes of turbulence evidently decrease at smaller scales.

The total turbulent amplitudes shown in Figures 9–11 represent the velocity dispersion averaged over the whole disk. For the purposes of assessing turbulent contributions to local disk stability, however, only the level of turbulence within a Jeans length $\sim c_s^2/(G\Sigma)$ is relevant. Furthermore, local observations of turbulence within the Milky Way generally measure velocity dispersions on scales less than the disk thickness. Thus, it is useful to estimate the turbulent amplitudes at smaller scales than the whole disk. We do this by running a window (or “beam”) of 1 kpc or 100 pc over the map and finding the dispersion of the velocity within this window at locations separated by the window size. When all zones within the window are weighted equally (as is true for the velocity power spectrum), we find that the mean velocity dispersions for model Q1D on scales of 1 kpc and 100 pc are 18 and 6.5 km s^{-1} , respectively. When we weight by mass, the respective velocity dispersions are 31 and 10 km s^{-1} . The larger values obtained when weighting by mass are indicative of the importance of dense expanding shells in driving the turbulence.

Since turbulence adds to the total momentum flux (the ram pressure acts similarly to the thermal pressure), a common assumption is that the sound speed c_s can be replaced by

$$c_{\text{eff}}^2 = c_s^2 + \sigma_R^2 \quad (19)$$

in the dispersion relations that characterize stability to axisymmetric modes, where σ_R is the radial component of the velocity dispersion. For models Q1SC and Q1SD, which have high P_{rad} , we find that the mean values of σ_R on kpc scales are 17 and 18 km s^{-1} , respectively. For the corresponding models Q1SB and Q1SE that have low P_{rad} , on the other hand, the values of σ_R on kpc scales are 10 and 8 km s^{-1} , respectively. Thus, the values of c_{eff} exceed c_s by a factor 1.6 for the low-turbulence models, whereas this increases to a factor 2.7 for the high-turbulence models. Our results discussed above indicate a decrease in the star formation rate with increasing c_{eff} ; we discuss theoretical ideas related to this finding in § 3.3.3 below.

3.3.2. Kennicutt-Schmidt Law

Figure 14 shows the local star formation rate per area as a function of mean surface density. To obtain these points, simulation data were binned in radius and time, with bins of widths 1 kpc and 18 Myr, respectively. Only models with a sufficient number of points, which is dependent to some degree on the number of feedback events, are shown. Best-fit lines to the data points are also shown. The rates show considerable scatter, both between models with different parameters as well as among points from a given model. However, where a large dynamic range is available, as is the case for the Q1D model and its extension to smaller radii (see below), a power-law relation $\Sigma_{\text{SFR}} \propto \Sigma^{1+p}$ is quite clear.

The $Q_0 = 1$ models, both with and without a spiral perturbation, and with different feedback parameters, generally give slopes $1 + p \sim 1$ –3. Most of the $Q_0 = 1$ models evolve for sufficiently long times that gas in the first clouds that are formed is allowed to be recycled into subsequently formed clouds several times. The $Q_0 = 2$ models, on the other hand, give a variety of

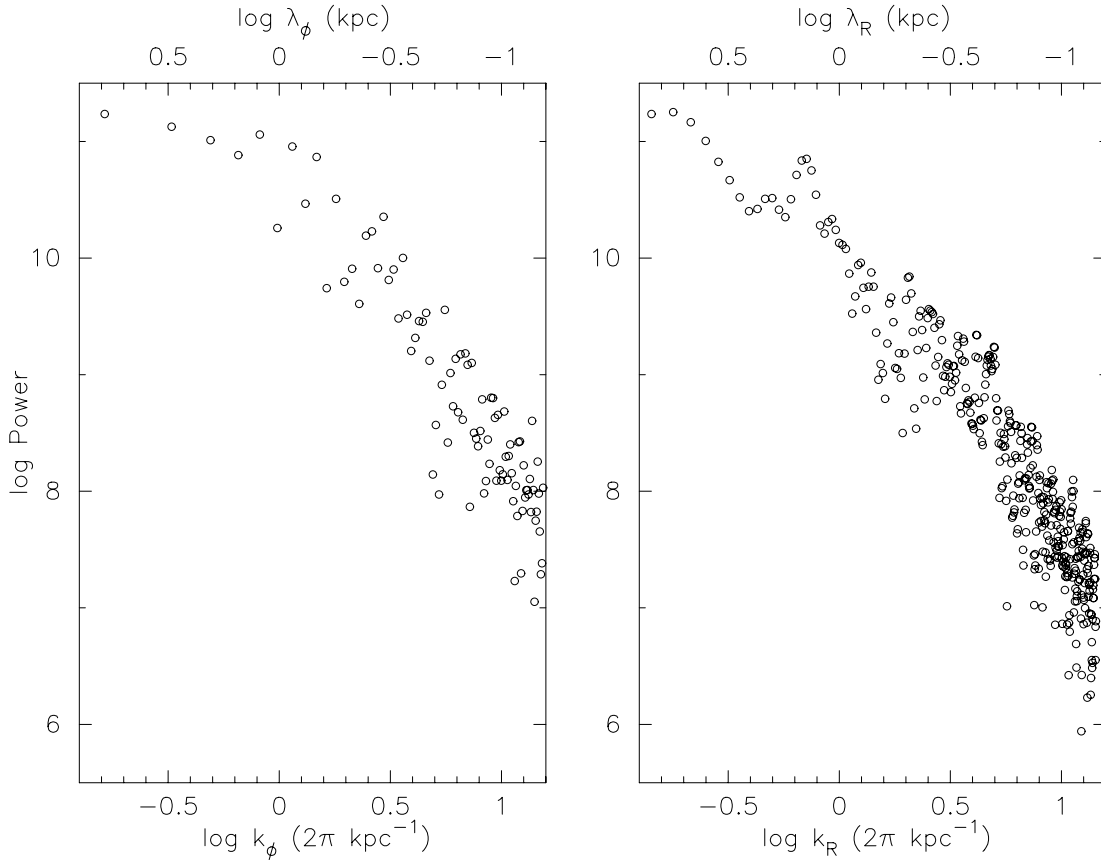


FIG. 13.— Turbulent power spectra of model Q1D. Power is shown at constant k_R (left) and constant k_ϕ (right; each slice is along the minimum nonzero value of the respective k). To obtain the dimensions of k_ϕ ($k_\phi = mn_\phi/R$), we use the mean radius of the grid. Best fits for values between $\log(k) = 0$ and 1 give slopes of -2.9 (left) and -2.4 (right).

slopes, and the relationship between the star formation rate and surface density is not as well correlated as in the $Q_0 = 1$ models. For the $Q_0 = 2$ models, the number of feedback events is insufficient to affect much of the disk. As a result, some clouds continue to collapse, and the Courant condition would demand an extremely small time step; at this point, we halt the simulation. Since the stochastic feedback events do not result in developed turbulence and a steady state is not approached in the $Q_0 = 2$ models, the SFR as computed is sensitive to model parameters governing the feedback events.

For some of our models, we have also run simulations of the inner regions of disks, with radial extent $R \in [0.8, 2.2]$ kpc. The other parameters are the same as for the standard models. The only difference here, besides the radial range, is the initial surface density. Since Q_0 is constant and $\Sigma_0 \propto (Q_0 R)^{-1}$, the initial surface density at all radii is increased by a factor 5 compared to the standard models with $R \in [4, 11]$ kpc.

Figure 15 shows the star formation rate as a function of surface density for model Q1D together with the corresponding inner region model. The larger surface density does indeed lead to higher star formation rates, with a slope $1 + p = 2.2$ that is similar to the value $1 + p = 2.4$ of the standard model. We find similar trends for other inner disk models in comparison with the corresponding standard models. For comparison, Figure 15 also shows data from Kennicutt (1998b). Each point indicates the globally averaged star formation rate for individual galaxies or their central regions (for starbursts). Although there is less scatter in the simulation points, the slope of the $\Sigma_{\text{SFR}} - \Sigma$ relation from the simulations (~ 2.3) is larger than the slope from observational data

($1 + p \sim 1.4$). At the low- Σ end, the model results overlap with the observed points.

3.3.3. Predicting Star Formation Times

The star formation (or gas depletion) time t_{SF} for the whole gaseous component of a galaxy is the time required for all the gas to be converted to stars if the star formation proceeds as it has been during a given interval Δt ,

$$t_{\text{SF}} = \Delta t \frac{M_{\text{tot}}}{\epsilon_{\text{SF}} \sum M_{\text{cl}}}, \quad (20)$$

where M_{tot} is the total mass in a given annulus. This quantity can be measured in our simulations; the summation in equation (20) is taken over all clouds in which a feedback event has occurred, as in equation (17).

Observationally, if the SN rate per dense gas mass R_{SN} is known, the star formation (or gas depletion) time can also be estimated based on the total amount of gas and the portion in dense clouds as

$$t'_{\text{SF}} = \frac{M_{\text{tot}}}{M_{\text{dense}} M_{\text{SN}} R_{\text{SN}}}, \quad (21)$$

where M_{dense} is the total mass of gas above some chosen threshold density. Since $R_{\text{SN}} M_{\text{SN}} = \epsilon_{\text{SF}} / t_{\text{cl}}$ from equation (12), the results of equations (20) and (21) should agree on average. With our two parameter choices $R_{\text{SN}} = 1$ or 10 (in units $2 \times 10^{-11} M_\odot^{-1} \text{ yr}^{-1}$), this implies $t'_{\text{SF}} = (1 \text{ or } 0.1)(M_{\text{tot}}/M_{\text{dense}})5 \times 10^8 \text{ yr}$.

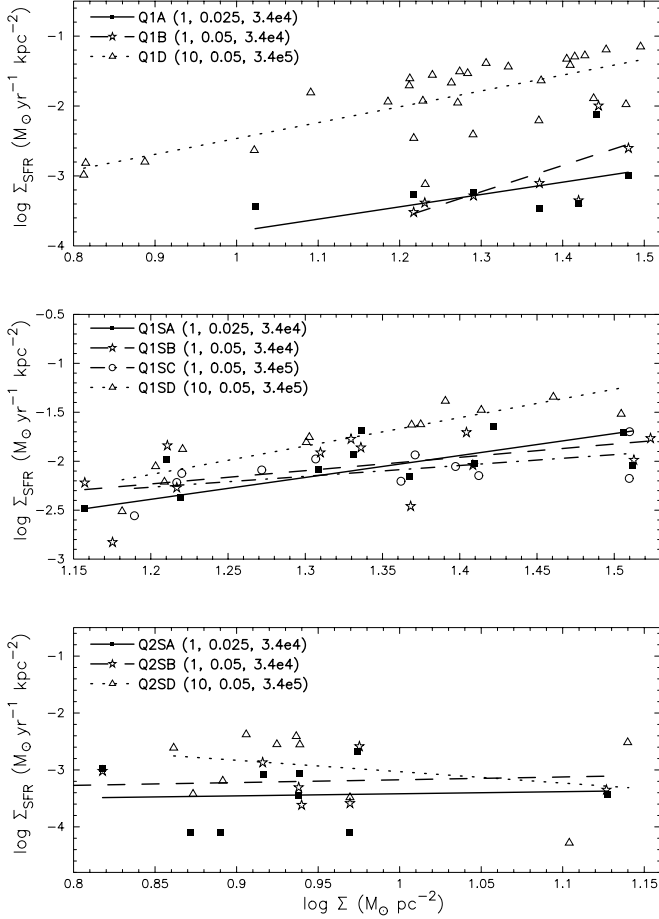


FIG. 14.—Schmidt law for models in Table 1. Each point is obtained by binning the simulation data in radii, with 1 kpc widths, and in time, with 18 Myr widths. Only annuli and times with at least one feedback event are included. The lines are the best fits to the points, with their slopes ranging from 1.8 to 3.8 (top), from 1.1 to 3.0 (middle), and from -2.0 to 1.9 (bottom).

We note that if the star formation or gas depletion time were computed only for *dense* gas (with local surface density $\gtrsim 200 M_{\odot} \text{pc}^{-2}$), then for our prescription it would simply be equal to a constant, $t'_{\text{SF}}(\text{dense}) = (M_{\text{SN}} R_{\text{SN}})^{-1} = 5 \times 10^7$ or 5×10^8 yr for $R_{\text{SN}} = 10$ or 1, respectively.

Figure 16 shows the star formation time in different radial annuli for model Q1D, as a function of Σ . The actual times, shown by the filled symbols, are computed using equation (20), after binning the simulation data in radii of 1 kpc widths and in time with $t/t_{\text{orb}} = 0.125$ widths. The open symbols show the predicted times by applying equation (21) on the same binned data. The predicted times agree well with the actual times. We find similar agreement with all other models.⁸ We also tested the correlation between t_{SF} and t_{orb} and found no strong correlation. This lack of correlation occurs because at later times the surface density profile no longer resembles the initial R^{-1} profile.

What is expected, on theoretical grounds, for the value of the star formation time? Consider the case in which gas cycles between diffuse (gravitationally unbound) and dense (gravitationally bound) components. The diffuse component forms dense clouds at a rate $M_{\text{diff}}/t_{\text{diff}}$, and the dense clouds are returned to the diffuse component plus stars over a cloud lifetime at a rate $M_{\text{dense}}/t_{\text{cl}}$.

Here M_{diff} and M_{dense} are the total diffuse and dense gas masses in an annulus, with corresponding surface densities when averaged over the area of Σ_{diff} and Σ_{dense} (the latter is not to be confused with the surface density of an individual dense cloud, which is much higher). Similarly, Σ is the surface density corresponding to the total mass of all the gas M_{tot} in an annulus. In equilibrium, the rates into and out of the dense component are equal, so that the star formation rate per unit area averaged over the annulus is

$$\begin{aligned} \Sigma_{\text{SFR}} &= \epsilon_{\text{SF}} \frac{\Sigma}{t_{\text{diff}} + t_{\text{cl}}} = \epsilon_{\text{SF}} \frac{\Sigma_{\text{diff}}}{t_{\text{diff}}} = \epsilon_{\text{SF}} \frac{\Sigma_{\text{dense}}}{t_{\text{cl}}} \\ &= R_{\text{SN}} M_{\text{SN}} \Sigma_{\text{dense}}. \end{aligned} \quad (22)$$

Including all the gas, the star formation timescale using the definition of equation (21) (and dropping the prime) is then

$$t_{\text{SF}} = \frac{t_{\text{diff}} + t_{\text{cl}}}{\epsilon_{\text{SF}}} = \frac{t_{\text{diff}}}{\epsilon_{\text{SF}}} \frac{M_{\text{tot}}}{M_{\text{diff}}} = \frac{t_{\text{cl}}}{\epsilon_{\text{SF}}} \frac{M_{\text{tot}}}{M_{\text{dense}}}. \quad (23)$$

Since $t_{\text{cl}}/\epsilon_{\text{SF}} = (R_{\text{SN}} M_{\text{SN}})^{-1} = 5 \times 10^7$ or 5×10^8 yr is held constant within any given model, the star formation time for all gas in an annulus is inversely proportional to the fraction of the gas above the density threshold in that annulus. If most of the gas is diffuse (as is true in our simulations), then $t_{\text{diff}} \gg t_{\text{cl}}$ and $t_{\text{SF}} \sim t_{\text{diff}}/\epsilon_{\text{SF}}$; the star formation time is set by the typical time required for diffuse gas to collect into bound clouds.

What characteristic values might be predicted for the cloud formation timescale, t_{diff} ? The shortest possible timescale would be that associated with the fastest growing Jeans modes in a disk. For a disk with semithickness H and sound speed c_s , the approximate dispersion relation for in-plane modes is $\omega^2 = k^2 c_s^2 - 2\pi G \Sigma |k| / (1 + |k|H)$ (Kim et al. 2002; Paper I). For the fastest growing modes (which satisfy $d|\omega^2|/dk = 0$) and for $H < c_s^2 / (\pi G \Sigma)$ (i.e., less than the thickness of an isothermal disk bound only by its own gravity), the inverse of the growth rate is $0.3t_J - 0.5t_J$, where $t_J = c_s / (G\Sigma)$ is the thin-disk Jeans length divided by c_s . In reality, rotation, shear, and turbulence must all affect the cloud growth timescale (see below), but the Jeans time nevertheless provides a useful reference value.

Another reference value for a structure formation timescale that is frequently used is the free-fall time, $t_{\text{ff}} = (3\pi/32G\rho)^{1/2}$. If the surface density and volume density are related via $\Sigma = \rho H (2\pi)^{1/2}$ (as for a Gaussian density distribution), then $t_{\text{ff}} = (3\sqrt{2}\pi^{3/2} H / 32G\Sigma)^{1/2}$. For our “thick-disk” Poisson solver, $H \propto R$ is adopted, so that $t_{\text{ff}} \propto (R/\Sigma)^{1/2}$. Our initial profiles follow $R \propto \Sigma^{-1}$, so that in the initial conditions $t_{\text{ff}} \propto \Sigma^{-1} \propto t_J$. In particular, for the $Q = 1$ case, $t_{\text{ff}} = 0.3t_J$ everywhere initially. Over time, however, the surface density is spatially rearranged, so that the values of t_J and t_{ff} are no longer strictly proportional.

Figure 17 shows the relationships between the star formation time and the reference values t_J and t_{ff} . While a clear correlation is evident for both relations, we find that there is less scatter in the $t_{\text{SF}}-t_J$ relation than in the $t_{\text{SF}}-t_{\text{ff}}$ relation. Further, many of the data points are consistent with a linear relationship $t_{\text{SF}} = 7t_J$, as indicated in the figure. If we compare to the prediction $t_{\text{SF}} = t_{\text{diff}}/\epsilon_{\text{SF}}$ and substitute the value $\epsilon_{\text{SF}} = 0.05$ used in model Q1D, this yields $t_{\text{diff}} = 0.35t_J$, which agrees with the simple estimate described above based on self-gravitating instabilities in thick disks. This result suggests that, provided the efficiencies of star formation in GMCs are constant and the disk is dominated by diffuse gas, the Jeans time in the diffuse gas controls the rate of star formation. While this result is quite intriguing, a high

⁸ Most other models do not run for as long as the D models that have high feedback rates, because some dense clumps continue to collapse without feedback, eventually causing the Courant condition to be violated.

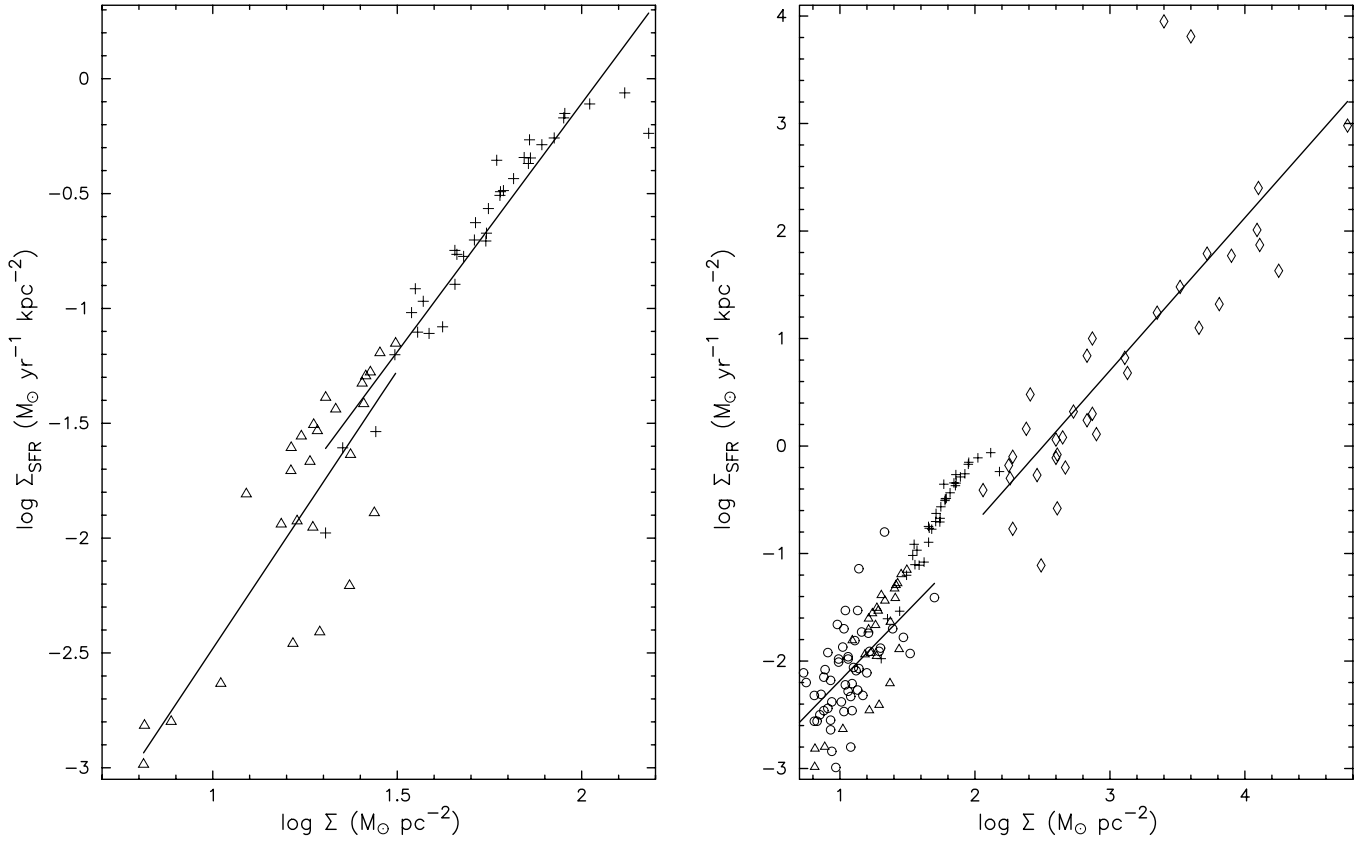


FIG. 15.—*Left*: Star formation rate vs. surface density for model Q1D (triangles; $R \in [4, 11]$ kpc), as well as the corresponding model of the inner region (crosses; $R \in [0.8, 2.2]$ kpc). Best-fit lines for each model are also shown, with slopes of 2.4 for the 4–11 kpc model and 2.2 for the 0.8–2.2 kpc model. *Right*: Triangles and crosses from the left panel are shown, along with globally averaged observational data from Kennicutt (1998b); circles show normal spirals, with best-fit slope of 1.3, and diamonds show IR starburst sources, with best-fit slope of 1.4.

dynamic range in a wider range of disk models is necessary to further investigate this relationship.

We note that in the dispersion relation used to predict $t_{\text{diff}} \sim t_J = c_s/(G\Sigma)$, no account was made for turbulence. As discussed in § 3.3.1, the simplest phenomenological modification of this relation would simply be to substitute $c_s \rightarrow c_{\text{eff}}$ (see eq. [19]). The results presented in § 3.3.1 which compare SFRs for model pairs with low and high P_{rad} , and hence different c_{eff} , are at least

semiquantitatively in support of this prescription for modifying t_J . There, we found that an increase of c_{eff} by a factor of ~ 2 is associated with a decrease in the SFR by a factor ~ 3 . However, the current models are not sufficient for a definitive statement. An important objective for future work is to test the relation between t_{SF} and the turbulence level using a more extensive set of models; the velocity dispersion can be varied by tuning the parameter P_{rad} . A fundamental understanding of star formation

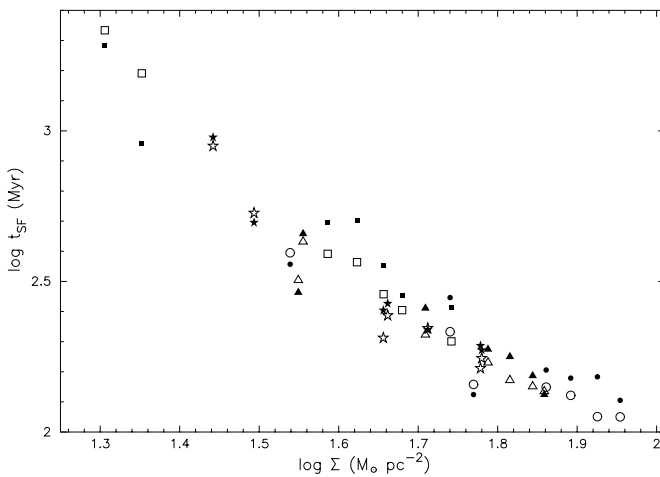


FIG. 16.—Star formation times from model Q1D, as a function of mean surface density. Different symbols correspond to different time bins of width 18 Myr. Simulation data are also binned in radii with widths of 1 kpc. Filled symbols show actual depletion times (eq. [20]), and open symbols show predicted depletion times (eq. [21]), for each annular and temporal bin.

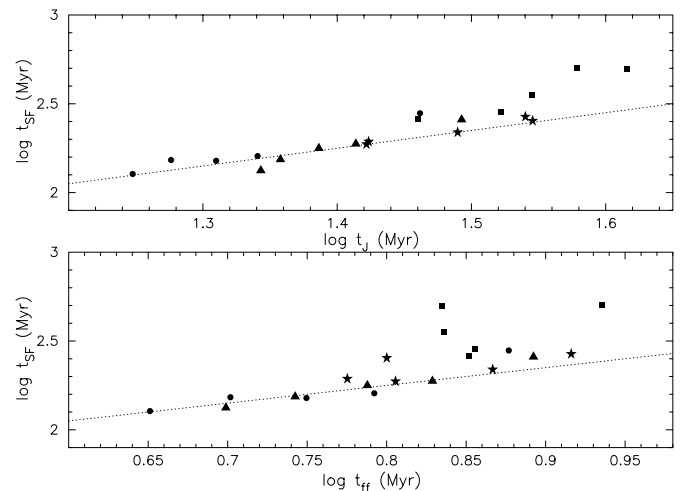


FIG. 17.—Star formation times from model Q1D, as a function of Jeans time (top) and free-fall time (bottom). Simulation data are binned as described in the caption to Fig. 16, with the innermost and outermost annuli excluded. The dashed lines, shown for comparison, have slopes of 1.

in molecular-dominated regions of galaxies (where the thermal velocity dispersion is dwarfed by the turbulent value) will depend on such investigations.

Modeling truly three-dimensional disks, with the vertical dimension fully resolved, would allow for a more complete study of the correlations between t_{SF} and the two gravitational times, t_{J} and t_{ff} . Depending on the regime, vertical hydrostatic equilibrium (for an isothermal medium) may be in the limit dominated by (1) the disk's gaseous self-gravity, so that the effective thickness of the ISM is $\Sigma/(2\rho_0) = c_s^2/(\pi G\Sigma)$, or (2) the disk's stellar gravity, so that the effective thickness is $\Sigma/(2\rho_0) = c_s\sigma_*/(2\sqrt{\pi G\Sigma_*}) \propto (Q_*/Q)c_s^2/(\pi G\Sigma)$. Here, σ_* and Σ_* are the stellar vertical velocity dispersion and surface density, respectively, and Q_* is the Toomre parameter for the stellar disk. Using these two forms, if gas dominates the vertical gravity, then $t_{\text{ff}} \propto t_{\text{J}}$, whereas if the stars dominate the vertical gravity, then $t_{\text{ff}} \propto t_{\text{J}}(Q_*/Q)^{1/2}$. If galaxies evolve such that Q_*/Q is constant, then $t_{\text{J}} \propto t_{\text{ff}}$ in either case; it would then be empirically difficult to establish whether t_{J} or t_{ff} is more fundamental for determining the star formation time. With explicit three-dimensional models, on the other hand, it will be possible to study the dependence of t_{SF} on t_{J} and t_{ff} separately, with Q_*/Q a tunable parameter. This represents a very interesting avenue for future research.

4. DISCUSSION AND SUMMARY

4.1. Kennicutt-Schmidt Law in Simulations

The prescription we adopt for star formation in this paper implies a constant relation between the mass (or mean surface density) of *dense* gas and the rate (or mean surface density) of star formation, $\Sigma_{\text{SFR}} = R_{\text{SN}}M_{\text{SN}}\Sigma_{\text{dense}}$. Using this prescription, we then test how the star formation rate scales with the surface density of *all* the gas. We find that our simulations are consistent with scalings $\Sigma_{\text{SFR}} \propto \Sigma^{1+p}$ for a range of power-law indices, but with significant scatter. In part, both the range of indices and the scatter in many of our models may arise from transient effects, rather than describing the behavior in a fully developed star-forming disk. Our simulations suggest that measured star formation properties are subject to transient effects; thus, for meaningful theoretical predictions it is necessary for systems to evolve well beyond the initial state.

For our strong-feedback model that most closely reaches an equilibrium between cloud formation and destruction and has a large dynamic range of surface density, we find a fairly tight relationship between Σ_{SFR} and Σ , with $1 + p \sim 2$ (see Fig. 15). This implies the fraction of dense gas follows $M_{\text{dense}}/M_{\text{tot}} = \Sigma_{\text{dense}}/\Sigma \propto \Sigma$. If we interpret this in terms of cloud formation/destruction equilibrium (cf. eq. [22]), with a constant mean cloud lifetime given by equation (12), this implies a dense gas formation time $\propto \Sigma^{-1}$. As discussed in § 3.3.3, our quantitative results are generally consistent with a formation time for dense gas $\propto t_{\text{J}}$ or t_{ff} , which vary (exactly or approximately) $\propto \Sigma^{-1}$ in our models.

In other recent numerical work, star formation prescriptions $\Sigma_{\text{SFR}} \propto \Sigma/t_{\text{ff}}$ have been adopted, where either all of the gas or just high-density gas is included in the right-hand side. This would imply $\Sigma_{\text{SFR}} \propto \Sigma^{3/2}(G/H)^{1/2}$ for the dependence on surface density and disk thickness. For a disk in vertical hydrostatic equilibrium with vertical velocity dispersion σ_z , the natural thickness varies as $H \propto \sigma_z^2/(G\Sigma)$, which would imply $\Sigma_{\text{SFR}} \propto \Sigma^2 G/\sigma_z$. Thus, a vertically resolved disk with a constant vertical velocity dispersion would be expected to yield an index $1 + p = 2$. If the disk thickness is determined not by hydrostatic equilibrium but in some other way, however, the resulting star formation rate and

the index in the Kennicutt-Schmidt law would depend on the numerical prescription (or physical process) that sets H . In our models, we have a flared disk $H \propto R$ and set $\Sigma \propto R^{-1}$ in our initial conditions, which accounts for the index $1 + p \sim 2$ that we obtain. If, on the other hand, the value of H were constant in a given simulation (either by design for a two-dimensional simulation or as a consequence of limited spatial resolution in a three-dimensional simulation), then the result would be $1 + p \sim 1.5$. Thus, limited vertical resolution can potentially artificially reduce the scaling index in the Kennicutt-Schmidt relation, as measured from numerical simulations. A fully resolved vertical dimension is therefore required if the star formation prescription is to be based on a volume density. In practice, the resolution requirement can be quite demanding if the disk is dominated by cold atomic or molecular gas, since $c_s^2/(\pi G\Sigma) = 4 \text{ pc}[T/(100 \text{ K})][\Sigma/(10 M_{\odot} \text{ pc}^{-2})]^{-1}$. This also points to the necessity of incorporating turbulent processes in three-dimensional models, since observed cold gas is in fact dominated by turbulent rather than thermal pressure. If these turbulent effects were not included, the disk thickness would be unphysically small.

4.2. Model Limitations and Future Prospects

4.2.1. Spiral Structure

In spiral models, the external spiral potential is initially the primary driver for enhancing the density, leading eventually to the growth of clouds. In models that evolve for a significant amount of time, soon after feedback and the dispersal of cloud gas the global spiral pattern is disrupted and eventually vanishes. With the simple feedback prescription that we have adopted, we were unable to simulate a spiral galaxy in which the global spiral pattern is maintained simultaneously as cloud gas is returned to the ISM through feedback.

If the arms truly are long lasting, then either the spiral potential is much stronger than in our models ($F \gg 10\%$) and/or the real feedback events are not as disruptive of structure on kpc scales. Very large F , however, does not appear consistent with observations of the old stellar disk (Rix & Rieke 1993). One possibility is that realistic feedback is both gentler and less correlated than the simple prescription of our current models, and as a consequence, the spiral arm coherence would not be destroyed by large-scale shells. Indeed, semianalytic models suggest that photoionization may evaporate much of the mass in a typical GMC before the pressure-driven expansion of H II regions unbinds the whole cloud (e.g., Krumholz et al. 2006). Those models do not include SNe, however, which are unavoidable if a GMC survives for more than one generation of OB stars. Still, SNe that are less correlated in space and time than the extreme case we have considered would disperse cloud gas in smaller parcels. Less correlated energy inputs would produce shells with diameters less than the spiral arm thickness and could more easily leave global spiral structure intact. By studying how the resulting spiral morphology varies with the correlation of feedback energy, it will be possible to place limits on how correlated star formation is in real galaxies.

4.2.2. Multiphase ISM

The models discussed in this paper use the simplest possible prescription for gas thermodynamics, which is an isothermal equation of state. Our adopted sound speed of $c_s = 7 \text{ km s}^{-1}$ corresponds to a temperature of $T \sim 10^4 \text{ K}$, characteristic of the warm phase of the ISM. We adopted this approach in order to investigate, in a controlled fashion, various separate effects that can contribute to the regulation of star formation.

In parallel with our simplified ISM thermodynamics, our approach to modeling feedback from star formation is also reduced to the most basic elements. In our models, we follow the expansion of clouds subsequent to correlated SN events. Of course, in a real SN event, thermal energy is injected into the ISM, and it is the expansion of a very hot and very diffuse bubble of gas that drives the formation of a dense shell around it. The cooling time in the high-density shell is short, so at late stages the isothermal approximation is adequate. The cooling time of the hot interior of each individual bubble, and of the hot phase of the ISM that results from merging SN remnants, is much longer. However, the hot phase contains only a very small fraction of the total ISM mass. From the point of view of most of the mass in the ISM, the primary effect of a SN is to inject momentum. By adopting an isothermal equation of state and treating feedback as providing momentum inputs, this effect is captured in an approximate way.

A significant limitation of our models is that we do not treat the cold ($T \sim 100$ K) atomic component of the ISM explicitly. Because the level of turbulence in the atomic component is comparable to the thermal velocity dispersion of warm gas (Heiles & Troland 2003), the effective pressure in the cold medium may be comparable to the thermal pressure in the warm medium. The dynamics associated with “turbulent pressure” may, however, be quite different from those resulting from microphysical thermal pressure. A very important direction for future work is to study directly how large-scale gravitational instabilities and spiral structure develop in multiphase, turbulent, cloudy gas.

Another limitation of our models is that they are two-dimensional (although the disk flares with radius). This constrains feedback energy to be confined within the galaxy’s midplane and does not allow for dynamically evolving disk thickness. In the real ISM, correlated SNe may be important in driving the SN-heated gas away from the midplane of the galaxy into the halo, through so-called chimneys and superbubbles (Norman & Ikeuchi 1989). To explore the effect of this energy loss in an approximate way, in our models we consider both a “standard” momentum input per SN and a momentum input reduced by a factor of 10. However, the cycling of gas through the galactic halo has other consequences as well. After this gas is cooled in the halo, it falls back onto the disk in the form of cloudlets (e.g., Joungh & Mac Low 2006). Even though recent simulations have shown that the fraction of mass that is vertically driven is small (e.g., de Avillez & Breitschwerdt 2004), the infalling clouds may still affect the dynamics of the disk and may also act as another source of turbulence.

In order to accurately model disks that account for the effects of SN heating, chimneys, superbubbles, and the return of halo gas onto the disk, a three-dimensional grid, as well as explicit treatment of heating and cooling, are necessary. Three-dimensional simulations will also allow us to test the sensitivity of the Kennicutt-Schmidt slope to the disk thickness (which evolves in response to star formation), as discussed in § 4.1. These directions are important avenues for future research.

4.3. Summary

In this paper we consider the formation of self-gravitating structures in global models of spiral galaxies, focusing on the effects of star formation feedback. Our numerical simulations adopt a simple, isothermal treatment of the gas and follow the flow in the disk by integrating the hydrodynamic equations on a polar grid. We incorporate vertical disk thickness effects within the solution of the Poisson equation, which assumes that the disk flares as $H \propto R$. The feedback model treats the specific star formation rate in gas above a given surface density threshold as

a constant, $R_{\text{SN}}M_{\text{SN}}$. Feedback is implemented by spatially resolved radial momentum injection subsequent to star formation events; the momentum injection is proportional to the number of stars formed. In order to explore the sensitivity of the resulting model properties to the feedback parameters, we consider a range of specific star formation rates, star formation efficiencies ϵ_{SF} , and momentum injection per massive star P_{rad} . We analyze the ISM spatial distribution, star formation rates, and turbulent properties of our model disks in cases with and without an externally imposed spiral gravitational perturbation.

Our main findings are as follows.

1. In models where P_{rad} is comparable to the level expected from a SN, clouds are destroyed by star formation events and the mean turbulence level is high. In models where P_{rad} is a factor of 10 lower, to represent inefficient feedback (e.g., if SN energy is vented vertically rather than kept in the disk), the self-gravitating structures that form are not destroyed by feedback, and the turbulence levels are substantially lower. Turbulence levels are insensitive to the star formation rate parameter R_{SN} and the overall star formation rate, however.

2. In models with strong feedback, expanding flows lead to collisions of shells, which then lead to gravitational collapse of overdense regions and further star formation events. In this sense, our models are a concrete realization of the concept of self-propagating star formation. We find, however, that the *net* effect of feedback is to *lower* the rate of star formation. That is, when we compare models with strong feedback (large P_{rad}) and weak feedback (small P_{rad}), the former have lower resultant star formation rates. Similarly, when we compare models (at large and fixed P_{rad}) that have high or low feedback event rates R_{SN} , the fraction of dense gas is lower when the event rate is higher. In principle, turbulence can either enhance collapse and star formation (by inducing shell collisions) or suppress collapse and star formation (by breaking up overdense regions). Our results show that although both effects occur, the latter dominates: star formation is in net suppressed by feedback.

3. For $\Sigma \sim 10\text{--}100 M_{\odot} \text{pc}^{-2}$, the range in Σ_{SFR} for our simulations is similar to the range observed in normal disks. The slope of the Kennicutt-Schmidt scaling relation $\Sigma_{\text{SFR}} \propto \Sigma^{1+p}$ is steeper ($1 + p \sim 2$) in our simulations than the slopes found from current observations at high (average) surface density. The discrepancy may be due to our assumption that the disk thickness varies with radius as $H \propto R$. Indeed, our numerical results are consistent with the theoretical prediction that $t_{\text{SF}} \propto t_{\text{J}}$ or t_{ff} when the gravitational times t_{J} and t_{ff} are calculated based on our model prescription. We point out that shallower scalings of Σ_{SFR} with Σ would be expected if the vertical velocity dispersion increases with Σ . This would increase the disk thickness at small radii (where Σ is large) relative to what we have assumed and, consequently, increase the gravitational times and reduce Σ_{SFR} .

4. Motivated by our own results, we remark that in general, the thickness of the gaseous disk in a galaxy (either observed or simulated) is important for setting the index in the Kennicutt-Schmidt relationship. Numerical simulations must resolve the natural disk scale height (set by pressure and turbulence) if the adopted prescription for star formation depends on the volume density ρ of gas. A simulation that is vertically unresolved ($H \rightarrow \text{const}$) while adopting $\rho_{\text{SF}} \propto \rho/t_{\text{ff}}(\rho)$, and hence $\Sigma_{\text{SF}} \propto \Sigma/t_{\text{ff}}(\rho)$, will automatically yield an index $1 + p = 1.5$ in the Kennicutt-Schmidt law since $t_{\text{ff}}^{-1} \propto (\Sigma/H)^{0.5}$. Fundamental understanding of Kennicutt-Schmidt laws requires a self-consistent determination of the dependence of H on Σ .

5. For turbulence driven by expanding shells in overdense regions, we find that the power spectra decrease with decreasing

size consistent with the scalings for shock-dominated flows (“Burgers turbulence”). While typical mass-weighted velocity dispersions on kpc scales in our high- P_{rad} models are 31 km s^{-1} , these decrease to 10 km s^{-1} on 100 pc scales. Radial and azimuthal components of the velocity dispersion in a given scale are comparable.

6. For all of our models, the maximum masses of dense clouds that form are several million M_{\odot} , consistent with observations of the upper cutoff in GMC/GMA mass distributions in local group galaxies. In models with strong turbulence, such that self-gravitating condensations can form in colliding flows, a wider range of cloud masses results, with a lower peak in the distribution (but similar upper cutoff). Higher resolution simulations will allow for a more detailed analysis of the mass distributions.

7. Within the context of the feedback prescription and parameters for our current set of models, we find that global spiral patterns are not maintained. For low P_{rad} , insufficient momentum is injected to overdense structures so that arm clouds continue to collapse, eventually depleting the surrounding spiral arm gas.

For high P_{rad} , large-scale expanding shells form and the global spiral structure is destroyed as cloud gas is dispersed. We conclude that highly correlated star formation, which is the limit that we adopt in the present models, is incompatible with long-lived spiral structure. It will be interesting to determine, by comparing spiral morphology with results from models adopting differing feedback prescriptions, what constraints are placed on the spatial and temporal correlation of star formation feedback in real galaxies.

This work was supported by grants 1278889 (NASA/*Spitzer*), and AST 05-07315 (NSF). Computations were performed on clusters supported by the Center for Theory and Computation in the Astronomy Department at the University of Maryland. For much of the data analysis and visualization, we have made use of NEMO software (Teuben 1995). We are also grateful to the anonymous referee for helpful comments.

APPENDIX

In the Appendix of Paper I we described two methods to solve Poisson’s equation numerically on a polar grid; both methods employ fast Fourier transforms (FFTs). One method sums the potential from concentric rings, as described by Miller (1976). The other method employs a coordinate transformation from polar coordinates to a Cartesian-like coordinate system. The former method is exact, but computationally expensive, and the latter is an approximation, but computationally efficient.

Here, we describe another FFT-based method that is exact and more efficient than the Miller (1976) method.⁹ The basic scheme is described in Kalnajs (1971) and Binney & Tremaine (1987); we describe a modification of Kalnajs’s method that includes the effect of nonzero disk thickness H , which also acts as softening.

The potential Φ at each position (R, ϕ) on the disk, at $z = 0$, is

$$\Phi(R, \phi, z = 0) = -G \int dR' \int d\phi' \int dz' \frac{R' f(z', R', \phi') \Sigma(R', \phi')}{[R'^2 + R^2 - 2RR' \cos(\phi - \phi') + z'^2]^{1/2}}. \quad (\text{A1})$$

Here, G is the usual gravitational constant, Σ is the total surface density, and the function $f = \rho(z', R', \phi')/\Sigma(R', \phi')$ describing the vertical profile of the volume density must be normalized, $\int_{-\infty}^{\infty} dz' f(z', R', \phi') = 1$. Substituting $u' \equiv \ln R'$ and $\zeta' = z'/\sqrt{2}R'$ in equation (A1), the potential reduces to

$$\Phi(R, \phi, z = 0) = -Ge^u \int du' \int d\phi' \int d\zeta' \frac{e^{u'-u} e^{u'} f(\zeta', u', \phi') \Sigma(u', \phi')}{\{e^{u-u'} [\cosh(u - u') - \cos(\phi - \phi')] + \zeta'^2\}^{1/2}}. \quad (\text{A2})$$

If $R' \rho(z', R', \phi')/\Sigma(R', \phi') = e^{u'} f(\zeta', u', \phi') \equiv g(\zeta')$ is a function of ζ' only (see below), we can define

$$I(u' - u, \phi' - \phi) \equiv e^{u'-u} \int d\zeta' \frac{g(\zeta')}{\{e^{u-u'} [\cosh(u - u') - \cos(\phi - \phi')] + \zeta'^2\}^{1/2}}. \quad (\text{A3})$$

Using the definition of I in equation (A2), we obtain Φ as a two-dimensional convolution,

$$\Phi(R, \phi, z = 0) = -Ge^u \int du' \int d\phi' \Sigma(u', \phi') I(u' - u, \phi' - \phi). \quad (\text{A4})$$

Applying the Fourier convolution theorem to equation (A4), the gravitational potential can be computed by taking the Fourier transform of Σ to obtain $\hat{\Sigma}$ and then taking the inverse Fourier transform of the product of $\hat{\Sigma}$ and \hat{I} , where \hat{I} is the Fourier transform of I . In hydrodynamic simulations, \hat{I} can be computed once at the beginning of the simulation run, so that only two FFTs need to be performed at each time step, $\text{FFT}(\Sigma)$ and $\text{FFT}^{-1}(\hat{\Sigma}\hat{I})$.

The function I , and therefore its convolution \hat{I} , depends on the normalized vertical distribution function $g(\zeta)$. For the specific case of a Gaussian vertical density distribution (which holds if the vertical gravity is dominated by that of the stellar disk),

$$f(z, R) = \frac{e^{-z^2/2H^2(R)}}{\sqrt{2\pi H^2(R)}}. \quad (\text{A5})$$

⁹ As in Paper I we again make use of the freely available FFTW software (Frigo & Johnson 2005).

For a disk that flares as $H(R) \propto R$, we define $\mathcal{H} = H(R)/R$, so that

$$e^u f(\zeta, R) = \frac{e^{-(\zeta/\mathcal{H})^2}}{\sqrt{2\pi}\mathcal{H}} \equiv g(\zeta). \quad (\text{A6})$$

Similarly, if the vertical density follows a sech^2 distribution (true if the gaseous self-gravity dominates), then $g(\zeta) = (2\mathcal{H})^{-1} \text{sech}^2(\zeta\sqrt{2}/\mathcal{H})$. For our simulations, we adopt the Gaussian profile; this yields the following explicit expression for I ,

$$I(u' - u, \phi' - \phi) \equiv \frac{e^{u'-u}}{\sqrt{2\pi}\mathcal{H}} \int_{-\infty}^{\infty} d\zeta' \frac{e^{-(\zeta'/\mathcal{H})^2}}{\{e^{u-u'} [\cosh(u - u') - \cos(\phi - \phi')] + \zeta'^2\}^{1/2}}. \quad (\text{A7})$$

Finally, we comment on the assumption $H(R) \propto R$ which enables the three-dimensional gravitational integral to be written as a two-dimensional convolution. If the stellar disk dominates gravity, then for an isothermal disk the vertical density distribution is Gaussian with $H/R = c_s Q_*(c_{*,z}/c_{*,R})/2v_c$, so values of c_s/v_c , Q_* , and $c_{*,z}/c_{*,R}$ that are independent of radius imply constant H/R . Similarly, if gas is the dominant component for vertical gravity, $H = c_s^2/\pi G\Sigma$, so that $H/R = c_s Q/\sqrt{2}v_c$. If both the Toomre Q parameter and c_s/v_c are independent of R , then $H/R = \text{const}$. For self-gravitating gaseous disks, if $Q = 1$ and $v_c/c_s = 30$, then $H/R = 0.02$. Including stellar gravity typically reduces H by a factor of ~ 2 (e.g., Kim et al. 2002).

For the simulations described in this paper, we use $H/R \equiv \mathcal{H} = 0.01$ in equation (A7). We have tested other values of \mathcal{H} and find that our results are not sensitive to the exact value. However, large changes significantly affect the rate of growth of self-gravitating perturbations.

REFERENCES

- Ballesteros-Paredes, J., Klessen, R. S., Mac Low, M.-M., & Vazquez-Semadeni, E. 2007, in *Protostars and Planets V*, ed. B. Reipurth, D. Jewitt, & K. Keil (Tucson: Univ. Arizona Press), 63
- Bertin, G., & Lin, C. C. 1996, *Spiral Structure in Galaxies: A Density Wave Theory* (Cambridge: MIT Press)
- Bigiel, F., et al. 2008, *AJ*, submitted
- Binney, J., & Tremaine, S. 1987, *Galactic Dynamics* (Princeton: Princeton Univ. Press)
- Blitz, L., Fukui, Y., Kawamura, A., Leroy, A., Mizuno, N., & Rosolowsky, E. 2007, in *Protostars and Planets V*, ed. B. Reipurth, D. Jewitt, & K. Keil (Tucson: Univ. Arizona Press), 81
- Boissier, S., et al. 2007, *ApJS*, 173, 524
- Bouche, N., et al. 2007, *ApJ*, 671, 303
- Chevalier, R. A. 1974, *ApJ*, 188, 501
- Cioffi, D. F., McKee, C. F., & Bertschinger, E. 1988, *ApJ*, 334, 252
- Cox, D. P., & Smith, B. W. 1974, *ApJ*, 189, L105
- de Avillez, M. A., & Breitschwerdt, D. 2004, *A&A*, 425, 899
- Elmegreen, B. G., & Elmegreen, D. M. 1983, *MNRAS*, 203, 31
- Elmegreen, B. G., & Scalo, J. 2004, *ARA&A*, 42, 211
- Elmegreen, D. M. 1980, *ApJ*, 242, 528
- Ferguson, A. M. N., Wyse, R. F. G., Gallagher, J. S., & Hunter, D. A. 1998, *ApJ*, 506, L19
- Frigo, M., & Johnson, S. G. 2005, *Proc. IEEE*, 93, 216
- Heiles, C., & Troland, T. H. 2003, *ApJ*, 586, 1067
- Heyer, M. H., Corbelli, E., Schneider, S. E., & Young, J. S. 2004, *ApJ*, 602, 723
- Joung, M. K. R., & Mac Low, M.-M. 2006, *ApJ*, 653, 1266
- Kalnajs, A. J. 1971, *ApJ*, 166, 275
- Kennicutt, R. C., Jr. 1989, *ApJ*, 344, 685
- . 1998a, *ARA&A*, 36, 189
- . 1998b, *ApJ*, 498, 541
- Kennicutt, R. C., Jr., et al. 2007, *ApJ*, 671, 333
- Kim, W.-T., & Ostriker, E. C. 2001, *ApJ*, 559, 70
- . 2002, *ApJ*, 570, 132
- . 2007, *ApJ*, 660, 1232
- Kim, W.-T., Ostriker, E. C., & Stone, J. M. 2002, *ApJ*, 581, 1080
- . 2003, *ApJ*, 599, 1157
- Knapen, J. H., Beckman, J. E., Cepa, J., & Nakai, N. 1996, *A&A*, 308, 27
- Kroupa, P. 2001, *MNRAS*, 322, 231
- Krumholz, M. R., Matzner, C. D., & McKee, C. F. 2006, *ApJ*, 653, 361
- La Vigne, M. A., Vogel, S. N., & Ostriker, E. C. 2006, *ApJ*, 650, 818
- Li, Y., Mac Low, M.-M., & Klessen, R. S. 2005a, *ApJ*, 620, L19
- . 2005b, *ApJ*, 626, 823
- . 2006, *ApJ*, 639, 879
- Lin, C. C., & Shu, F. H. 1964, *ApJ*, 140, 646
- Mac Low, M.-M., & Klessen, R. S. 2004, *Rev. Mod. Phys.*, 76, 125
- Martin, C. L., & Kennicutt, R. C., Jr. 2001, *ApJ*, 555, 301
- McKee, C. F., & Ostriker, E. C. 2007, *ARA&A*, 45, 565
- McKee, C. F., & Ostriker, J. P. 1977, *ApJ*, 218, 148
- Miller, R. H. 1976, *J. Comput. Phys.*, 21, 400
- Norman, C. A., & Ikeuchi, S. 1989, *ApJ*, 345, 372
- Rix, H.-W., & Rieke, M. J. 1993, *ApJ*, 418, 123
- Robertson, B., & Kravtsov, A. 2008, *ApJ*, 680, 1083
- Schmidt, M. 1959, *ApJ*, 129, 243
- Schuster, K. F., Kramer, C., Hitschfeld, M., Garcia-Burillo, S., & Mookerjee, B. 2007, *A&A*, 461, 143
- Shetty, R., & Ostriker, E. C. 2006, *ApJ*, 647, 997 (Paper I)
- Spitzer, L. 1978, *Physical Processes in the Interstellar Medium* (New York: Wiley-Interscience)
- Stone, J. M., & Norman, M. L. 1992a, *ApJS*, 80, 753
- . 1992b, *ApJS*, 80, 791
- Tasker, E. J., & Bryan, G. L. 2006, *ApJ*, 641, 878
- . 2008, *ApJ*, 673, 810
- Teuben, P. 1995, in *ASP Conf. Ser. 77, Astronomical Data Analysis Software and Systems IV*, ed. R. A. Shaw, H. E. Payne, & J. J. E. Hayes (San Francisco: ASP), 398
- Thilker, D. A., et al. 2007, *ApJS*, 173, 572
- Toomre, A. 1964, *ApJ*, 139, 1217
- Truelove, J. K., Klein, R. I., McKee, C. F., Holliman, J. H., II, Howell, L. H., & Greenough, J. A. 1997, *ApJ*, 489, L179
- Vogel, S. N., Kulkarni, S. R., & Scoville, N. Z. 1988, *Nature*, 334, 402
- Wada, K., & Norman, C. A. 2001, *ApJ*, 547, 172
- Wong, T., & Blitz, L. 2002, *ApJ*, 569, 157